CHAPTER 2

Synthesis, Crystal Features and Characterization of a series of Acylpyrazolone ligands: Computational analysis

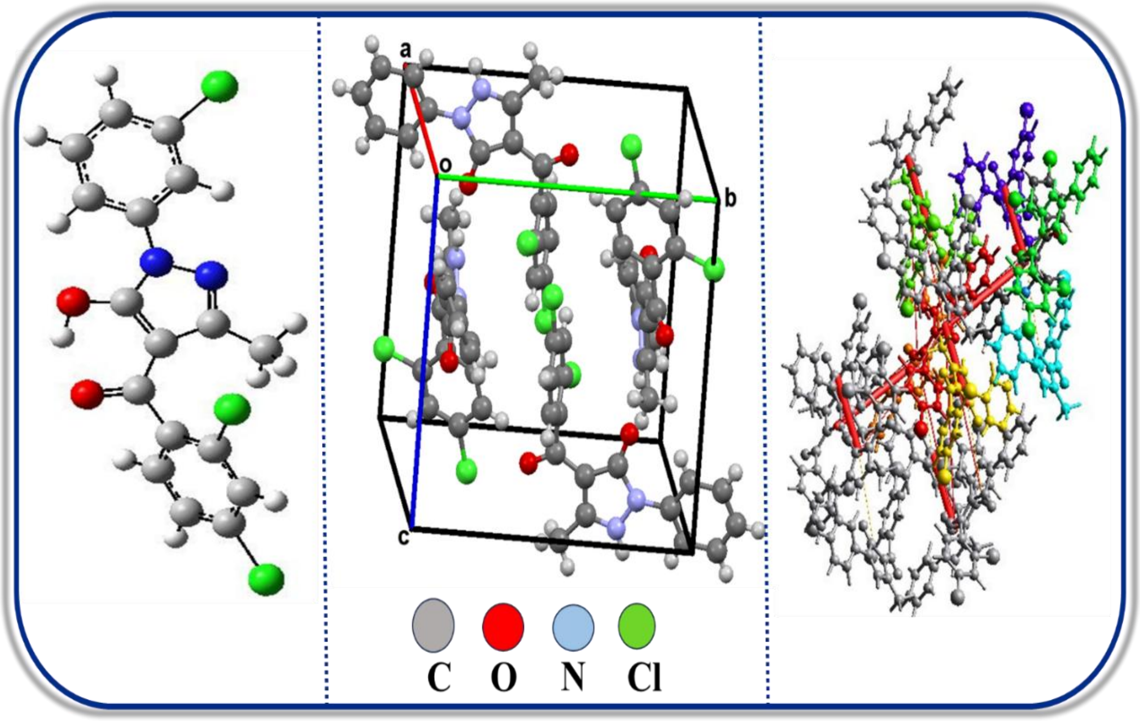

2.1 Introduction

As a key structural motif, pyrazolone is found in various bioactive compounds [1]. 4-Acylpyrazolones are derivatives of pyrazolone featuring diketone structures, with substitutions occurring at the pyrazole ring's fourth position. Due to tautomerism, these compounds can exist in both enol and keto forms; they can form various interesting coordination compounds. Due to their significant pharmacological and biological applications, acylpyrazolones have gained recognition as an increasingly important class of heterocycles [2]**.**

The acyl pyrazolone demonstrates a range of electrical, optical, and biological activities, making it an important subject in scientific research [1]. This compound is a key member of the pyrazolone family, known for its five-membered heterocyclic structure. Its unique appeal in coordination chemistry stems from two adjacent heterocyclic nitrogen atoms and an additional C=O group. Among these, derivatives of 4-acyl pyrazolone are particularly noteworthy, owing to their chelating arm featuring a β-diketone structure. As noted by Jensen [3], acylation predominantly occurs at the C-4 position of the pyrazole ring under basic conditions, such as when using calcium hydroxide in refluxing dioxane. Numerous acyl pyrazolone derivatives have been synthesized, primarily through functionalization at the C-4 position with the acyl (-COOR) group, followed by reactions with specific amines [1][4].

A recent review by Marchetti and colleagues has explored the various applications of pyrazolone-based transition metal complexes, the properties and uses of acylpyrazolone ligands, and their corresponding transition metal complexes [4][5]**.** Evaluating the crystal strength of acylpyrazolones using various characterization techniques is essential and highly informative for research. This assessment provides insights into the interaction energy and the degree of covalency within metal-ligand bonds, which are key factors that influence the properties of these complexes. Focusing on these aspects, we have synthesized acylpyrazolone-based copper and nickel complexes. Chapters **3, 4,** and **5** provide a complete explanation of these complexes. This chapter focuses primarily on the synthesis, crystal structure analysis, and comprehensive characterization of a series of acylpyrazolone ligands. In addition to the experimental investigations, computational techniques are employed to model and predict these ligands' electronic properties, stability, and reactivity. This combined approach provides a detailed understanding of their molecular behaviour and potential applications.

2.2 Experimental work

2.2.1 Materials and Methods

The starting materials, a pyrazolone was purchased from Sidhdhanath Industries in Sachin (Surat), India and 2,4-dichlorobenzoyl chloride was obtained from Shiva Pharmachem Limited in Vadodara (Gujarat), India. Dioxane was sourced from E. Merck (India) Ltd., and calcium hydroxide from LOBA Chem Pvt. Ltd., Mumbai. All the chemicals used in this study were purified using standard methods [6]. These materials were essential for the successful execution of the experiments and were acquired under the procurement guidelines.

2.2.2 Synthesis of ligands

All three ligands, HL^I, HL^{II} and HL^{III} were synthesized using the method suggested by Jensen [3]. In a three-necked round-bottom flask equipped with a mechanical stirrer, pyrazolone (the starting material) and 1,4-dioxane (40 mL) were added, along with two equivalents of calcium hydroxide, followed by the dropwise addition of 1 equivalent of “2,4-dichlorobenzoyl chloride” (R). The reaction mixture was then treated with 200 mL of 2M hydrochloric acid. The resulting product was recrystallized using rectified spirit. The synthetic pathway of HL^I, HL^{II} and HL^{III} ligands is depicted in **Fig.2.1.** A 2d representation and physical appearance of HL^I, HL^{II} and HL^{III} ligands are mentioned in **Fig.2.2.**

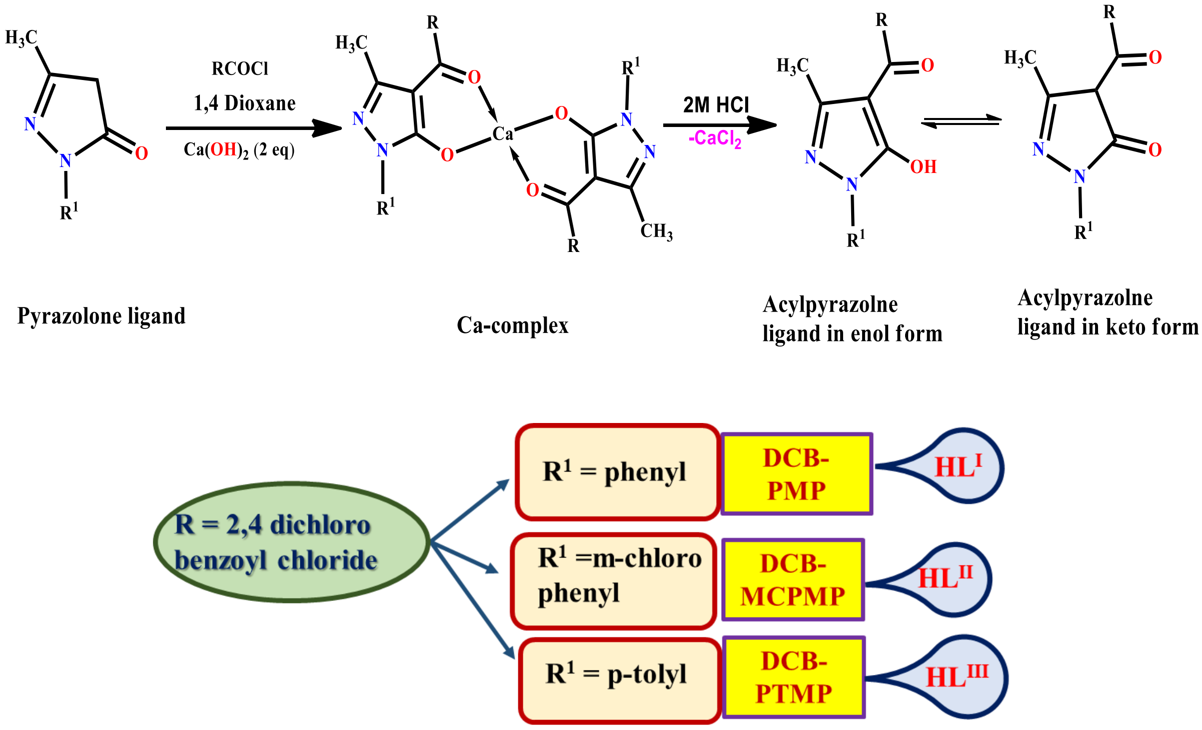

Fig.2.1. Synthetic route of HL^I, HL^{II} and HL^{III} ligands

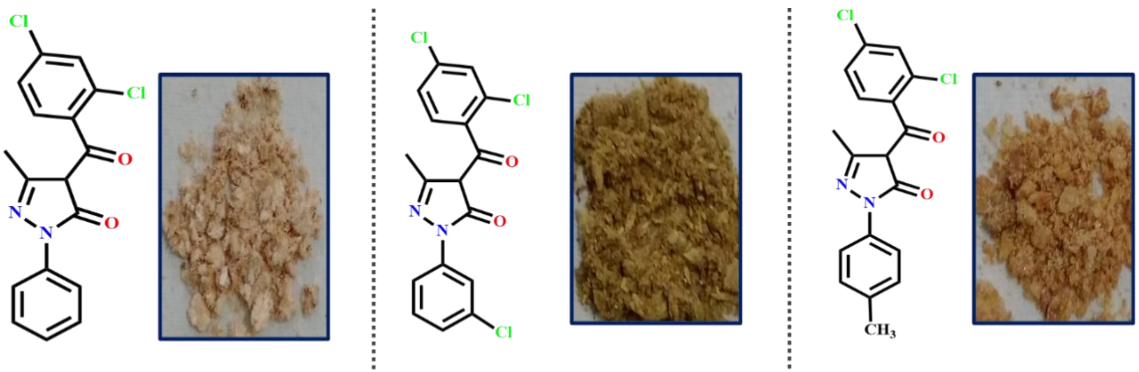

HL^I ligand HL^{II} ligand HL^{III} ligand

Fig.2.2. A 2d representation and physical appearance of ligands HL^I, HL^{II} and HL^{III}

HL^I ligand; (1-(3-chlorophenyl)-5-hyroxy-3-methyl-1H-pyrazol-4-yl)(2,4 dichlorophenyl)methanone):

1-phenyl-3-methyl-5-pyrazolone (0.05 mol, 8.7 g), and 2,4-dichloro benzoyl chloride (0.05 mol, 10.4 ml), **Colour:** Light creamish orange, **yield:** 85%, **M.P:** 128°C, **Molecular formula:** $C_{17}H_{12}Cl_2N_2O_2$, **M.W:** 347.20, **Elemental analysis**: C (Exp. 59.95%, Calc. 58.81%); H (Exp. 3.90%, Calc. 3.48%); N (Exp. 8.10%, Calc. 8.07%), **FTIR (KBr, cm^{-1}):** ν(C=O) of pyrazolone; (1627), ν(C=O) of 2,4 dichloro benzoyl; (1587), Cyclic ν(C=N); (1515), C–H in plane deformation; (1394), **NMR: ^{1}H NMR δ-ppm (400 MHz, $CDCl_3$):** 2.195 (s, 3H, CH_3(pyz)), 7.3–7.8 (m, Ar-H of HL^I ligand).

HL^{II} ligand; (2,5-dichlorophenyl)(5-hydroxy-3-methyl-1-phenyl-1H-pyrazol-4-yl) methanone:

m-chloro phenyl 3-methyl 5-pyrazolone (0.05 mol, 10.43 g), and 2,4-dichloro benzoyl chloride (0.05 mol, 10.4 ml), **Colour:** Light creamish orange, **yield:** 86%, **M.P:** 135°C, **Molecular formula:** $C_{17}H_{11}Cl_3N_2O_2$, **M.W:** 381.64, **Elemental analysis**: C (Exp. 54.10%, Calc. 53.50%); H (Exp. 3.05%, Calc. 2.91%); N (Exp. 7.50%, Calc. 7.34%), **FTIR (KBr, cm^{-1}):** ν(C=O) of pyrazolone; (1594), ν(C=O) of 2,4 dichloro benzoyl; (1550), Cyclic ν(C=N); (1482), C–H in-plane deformation; (1062), **^{1}H NMR δ-ppm (400 MHz, $CDCl_3$)**: d ppm:1.89 (s, 3H, Pyrazolone C-CH_3), 7.3–7.9 (m, Ar-H of HL^{II} ligand).

HL^{III} ligand;(2,5-chlorophenyl)(5-hydroxy-3-methyl-1-(*p*-tolyl)-1H-pyrazol-4-yl)methanone 3-methyl 5-pyrazolone):

p-tolyl 3-methyl 5-pyrazolone (0.05 mol, 9.41 g), and 2,4-dichloro benzoyl chloride (0.05 mol, 10.4 ml), **Colour: Orange-brown, yield:** 86%, **M.P:** 135°C, **Molecular formula:** $C_{18}H_{14}Cl_2N_2O_2$, **M.W:** 361.22, **Elemental analysis**: C (Exp. 60.12%, Calc. 59.85%); H

(Exp. 4.10%, Calc. 3.91%); N (Exp. 7.85%, Calc. 7.76%), **FTIR (KBr, cm^{-1}):** ν(C=O) of pyrazolone; (1668), ν(C=O) of 2,4 dichloro benzoyl; (1585), Cyclic ν(C=N); (1472), C–H in-plane deformation; (1253), **^{1}H NMR δ-ppm (400 MHz, $CDCl_3$)**: d ppm:1.94 (s, 3H, Pyrazolone C-CH_3), 7.4–7.7 (m, Aromatic-H of HL^{III} ligand).

Furthermore, ligands HL^{IV}, HL^{V}, HL^{VI}, HL^{VII}, HL^{VIII} and HL^{IX} were synthesized using a similar method as described in **Section 2.2.2**. '*p*-chloro benzoyl chloride' (R) was used to synthesize the HL^{IV}, HL^{V} and HL^{VI} ligands. In contrast, '3,5-dimethyl benzoyl chloride' (R) and '*p*-nitro benzoyl chloride' (R) were used to synthesise HL^{VII}, HL^{VIII} and HL^{IX} ligands. Ligands HL^{IV}, HL^{V} and HL^{VI} [7][8]**,** HL^{VII} and HL^{VIII} [9][10] and HL^{IX} ligand [11] have been reported previously by our lab. A 2d representation of ligands HL^{IV}-HL^{IX} is shown in **Figs.2.3-2.4**.

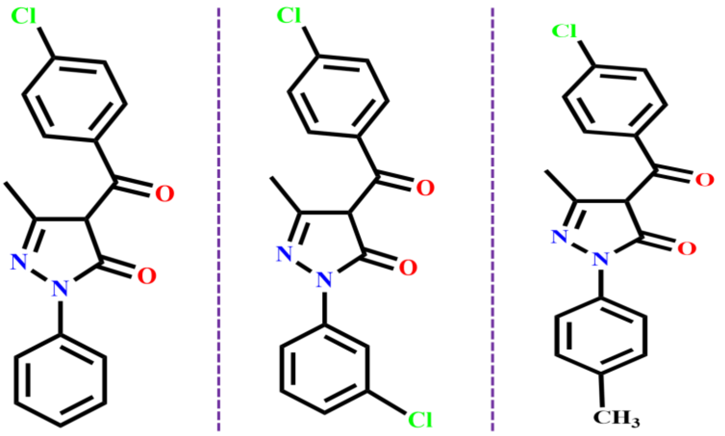

HL^{IV} ligand **HL^{V} ligand** **HL^{VI} ligand**

Fig.2.3. A 2d representation of ligands HL^{IV}, HL^{V} and HL^{VI}

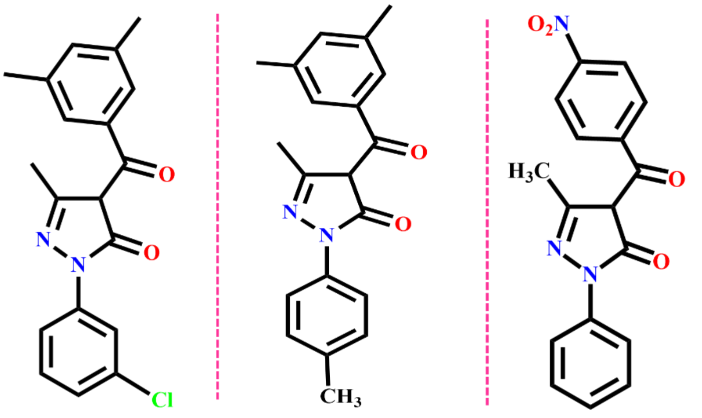

HL^{VII} ligand **HL^{VIII} ligand** **HL^{IX} ligand**

Fig.2.4. A 2d representation of ligands HL^{VII}, HL^{VIII} and HL^{IX}

2.2.3 X-ray crystallographic study

X-ray quality single crystals of all three synthesized ligands, HL^I, HL^{II} and HL^{III} were obtained in rectified spirit. X-ray diffraction data were recorded at 298(2) K for HL^I and HL^{II} ligands and at 100(2) K for HL^{III} ligand, using a Bruker APEX-II CCD diffractometer with Cu—Kα radiation ($\lambda = 1.54178$ Å) and a graphite monochromator. The diffraction data were analyzed using the SHELXT programme for structure solution [12]. Refinement was carried out through full-matrix least squares methods based on F^2 with the SHELXL-2018/3 program [13]. A micro-focus sealed X-ray tube was used as the diffraction source. All non-hydrogen atoms were located in their expected positions within the structures. The ORTEP diagrams of the complexes were produced using Mercury software [14].

2.2.4 Physical measurements and characterization

The synthesized ligands were examined through analytical and spectroscopic techniques. A Bruker Alpha model recorded infrared spectra (4000-400 cm^{-1} KBr discs). The ^1H NMR spectra were recorded using a Bruker AV 400 MHz instrument, with $CDCl_3$ solvent and TMS as an internal reference. DFT computational analysis and Hirshfeld surface area analysis were also studied.

2.2.5 Computational analysis

Density functional theory (DFT) was used for full geometry optimization of the ligands with the help of Gauss View 6.0, a molecular visualisation software. For (DFT) calculations, a B3LYP functional was employed. This functional combines Becke's three-parameter exchange function with the correlation function proposed by Lee, Yang, and Parr. The 6-31G basis set, a split-valence type, was chosen for its optimal balance between computational efficiency and accuracy in modelling molecular geometries and electronic structures. The B3LYP/6-31G method is widely recognized for providing reliable results in the analysis of organic and coordination compounds, including predictions of bond lengths, bond angles, and vibrational frequencies. This combination strikes a suitable balance between computational cost and accuracy, making it well-suited for investigating larger molecular systems in this research. All the calculations, HOMO-LUMO energy gap and Global parameters were carried out in Gauss View 6.0 software using the same basis set. After the geometry optimization, the vibrational frequency calculations were conducted at the same computational level to assess the nature of the identified stationary points [15].

2.3 Results and Discussion

2.3.1 FTIR spectral analysis

FTIR spectroscopy is a non-destructive and highly valuable technique in coordination chemistry, crucial for providing detailed insights into metal-ligand interactions at the molecular level. By comparing the spectra of ligands with their corresponding metal complexes, infrared spectral investigations offer important information about the coordination sites of ligands. The FTIR spectra of ligands typically show characteristic peaks essential for understanding bonding and coordination changes. Therefore, only significant bands that have either changed or newly appeared are discussed here. In the FTIR spectra of the free ligands, the bands at 1627 cm^{-1}, 1594 cm^{-1} and 1668 cm^{-1} are assigned to the ν(C=O) stretching vibration of pyrazolone ring in the HL^{I}, HL^{II} and HL^{III} ligands, respectively. Conversely, the ν(C=O) bands for 2,4-dichlorobenzoyl chloride appear at 1587 cm^{-1}, 1550 cm^{-1} and 1585 cm^{-1} for HL^{I}, HL^{II} and HL^{III} ligands, respectively. Additionally, the frequencies of cyclic ν(C=N) and C-H in-plane deformation are significant and listed in **Table 2.1.** FTIR spectra of ligands HL^{I}, HL^{II} and HL^{III} are depicted in **Figs.2.5-2.7,** respectively.

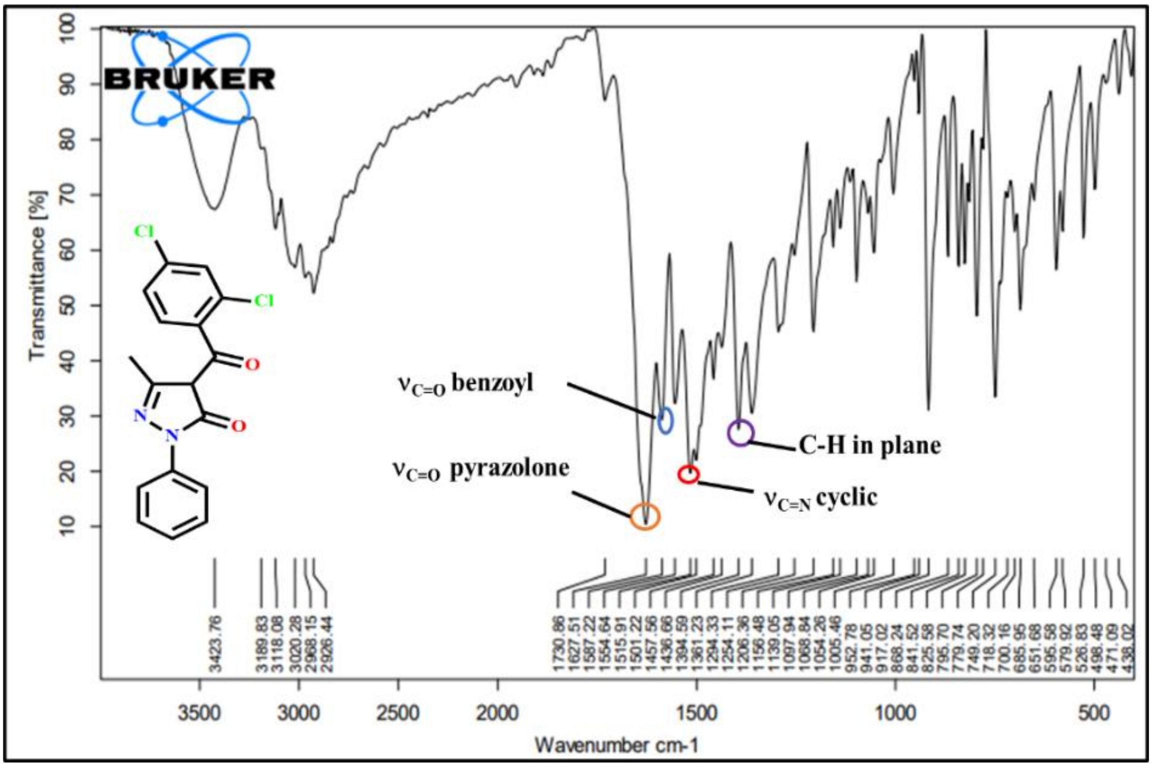

Fig.2.5. FTIR spectrum of HL^{I} ligand

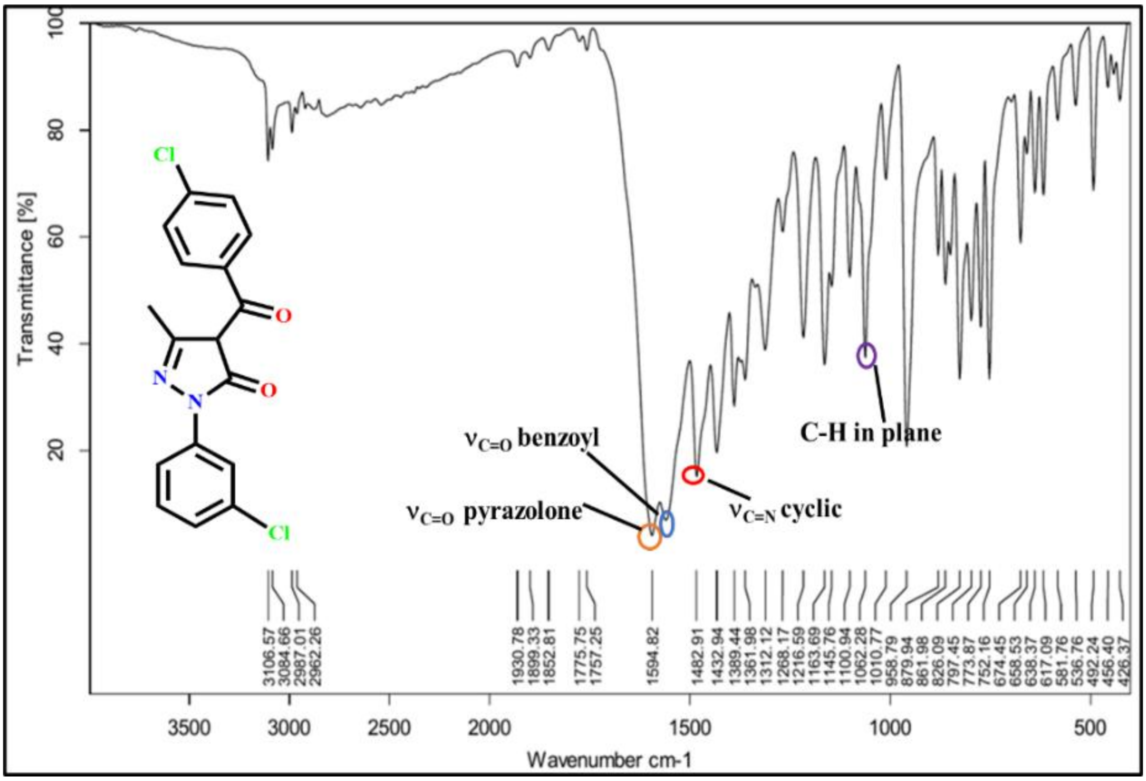

Fig.2.6. FTIR spectrum of HL^{II} ligand

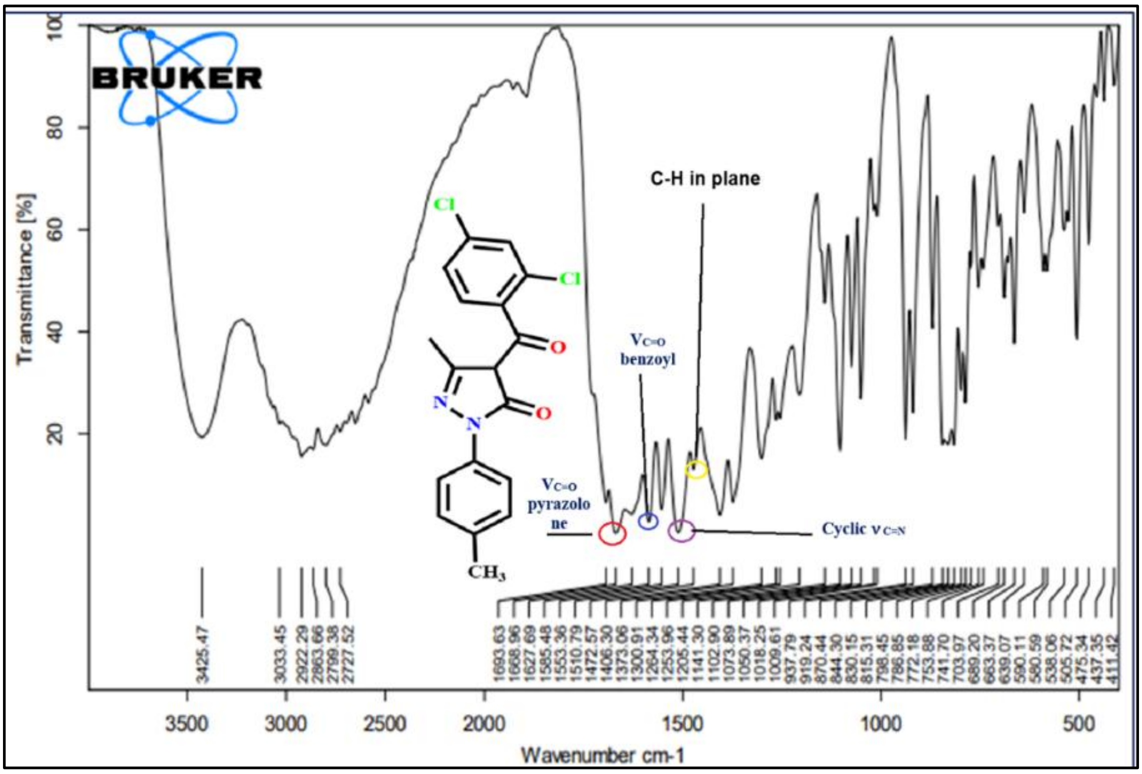

Fig.2.7. FTIR spectrum of HL^{III} ligand

Table 2.1. FTIR spectral data of ligands HL^{I}, HL^{II} and HL^{III}

Code	ν(C=O) of 2,4-dichloro benzoyl	ν(C=O) of Pyrazolone	Cyclic ν(C=N)	C-H in-plane deformation
HL^{I} ligand	1587	1627	1515	1394
HL^{II} ligand	1550	1594	1482	1062
HL^{III} ligand	1585	1668	1472	1253

2.3.2 ^{1}H-NMR spectral analysis

The ^{1}H-NMR spectra of all three ligands were recorded in $CDCl_3$ solvent. A singlet for a methyl proton of 3-methyl pyrazolone was observed at δ 2.19 ppm, 1.89 ppm and 1.90 ppm for the HL^{I}, HL^{II} and HL^{III} ligands, respectively. In the aromatic region between 7.28–7.94 δ ppm, several doublets were observed, with some overlapping doublets or multiplets due to aromatic protons. Various factors can influence the chemical shifts of exchangeable protons, including temperature, concentration, pH, water content, and solvent. These shifts occur due to chemical exchange, hydrogen bonding and conformational changes. Hydroxyl groups are particularly sensitive to these factors. More consistent chemical shifts can be obtained in non-polar solvents like DMSO, while exchangeable chemical shifts in $CDCl_3$ are often difficult to reproduce [16].

Therefore, the ^{1}H-NMR spectra of the three synthesized ligands in $CDCl_3$ align well with the proposed structures. The ^{1}H-NMR spectra of ligands HL^{I}, HL^{II} and HL^{III} are sequentially displayed in **Figs.2.8-2.10.**

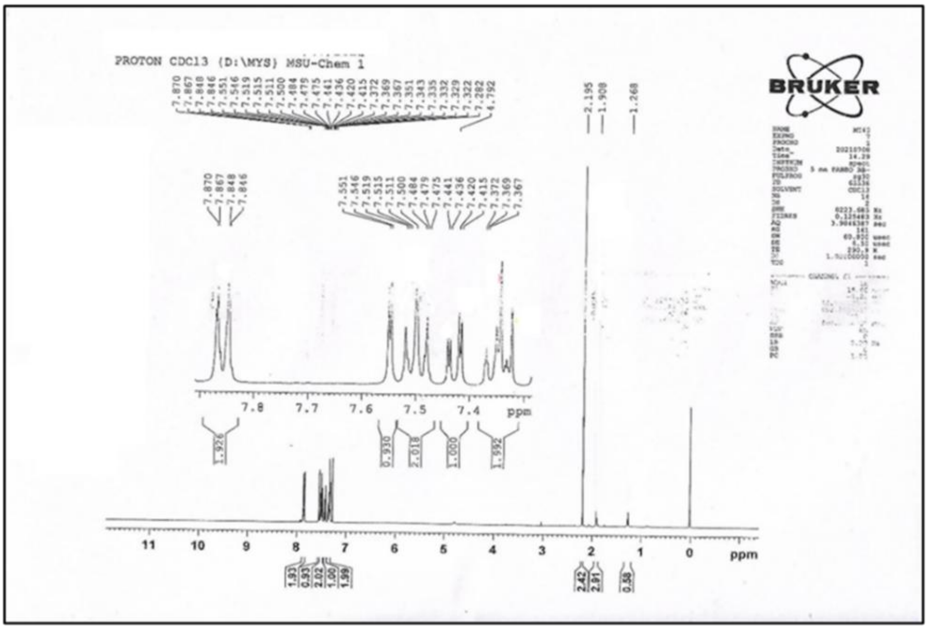

Fig.2.8. ^{1}H-NMR spectrum of HL^{I} ligand

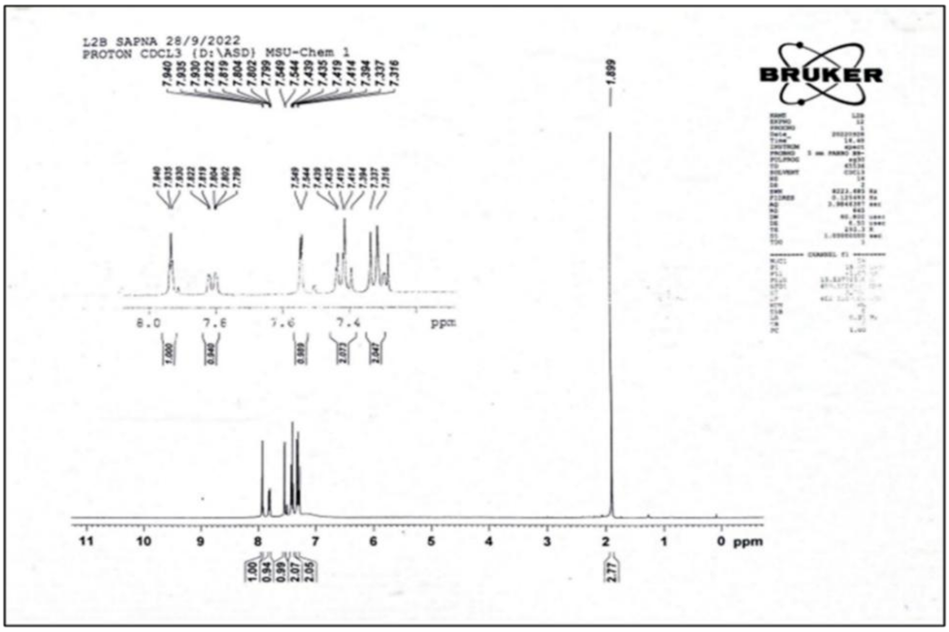

Fig.2.9. ^{1}H-NMR spectrum of HL^{II} ligand

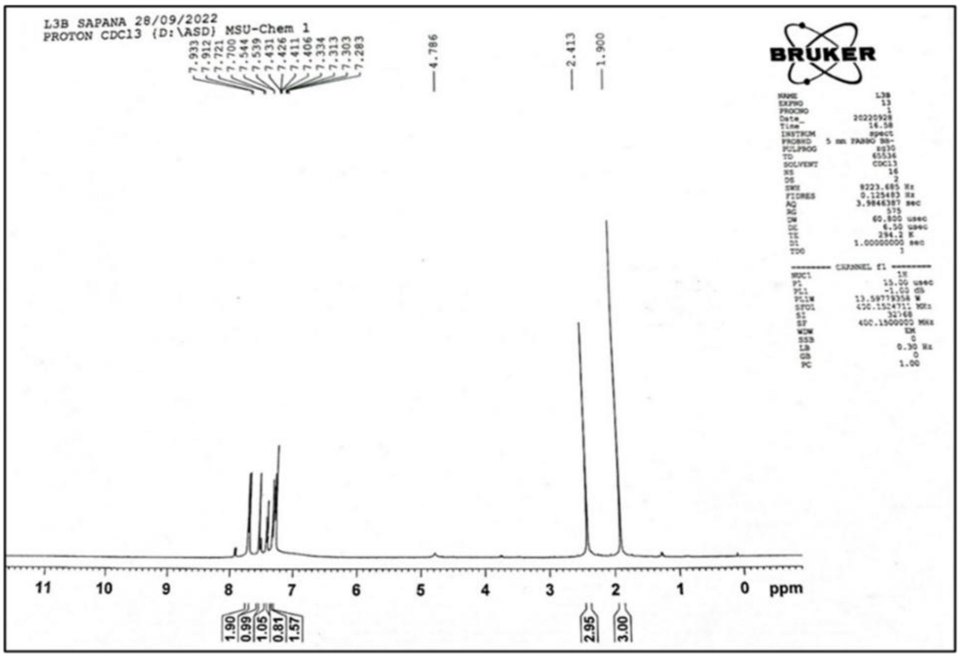

Fig.2.10. ^{1}H-NMR spectrum of HL^{III} ligand

2.3.3 Single crystal X-ray diffraction analysis

(i) Molecular crystal Structure of HL^{I} ligand

The HL^{I} ligand was recrystallized from the rectified spirit, resulting in a colourless, transparent crystal in the keto form, as confirmed by single crystal diffraction analysis. The ligand crystallizes in the **'Triclinic *P*-1'** space group. The characteristic C=O bond lengths of the ligand are 1.221(4) Å for the C(11)-O(2) bond of the 2,4-dichlorobenzoyl group and 1.242(3) Å for the C(10)-O(1) bond of the pyrazolone, both of which are close to the typical

C=O double bond length [17]. Additionally, the C(7)-N(2) bond, measuring 1.323(4) Å, is close to the typical bond length for C=N double bonds [18]. The characteristic bond lengths of C(13)-Cl(1) and C(15)-Cl(2) are 1.731(3) Å and 1.737(3) Å, respectively. The molecular crystal structure and crystal packing of the HL^I ligand are shown in **Fig. 2.11**. The significant bond lengths and bond angles parameters for the HL^I ligand are provided in **Table 2.2.** The relevant hydrogen bonding parameters, along with the associated symmetry transformations, are presented in **Table 2.3 and Table 2.4**, respectively

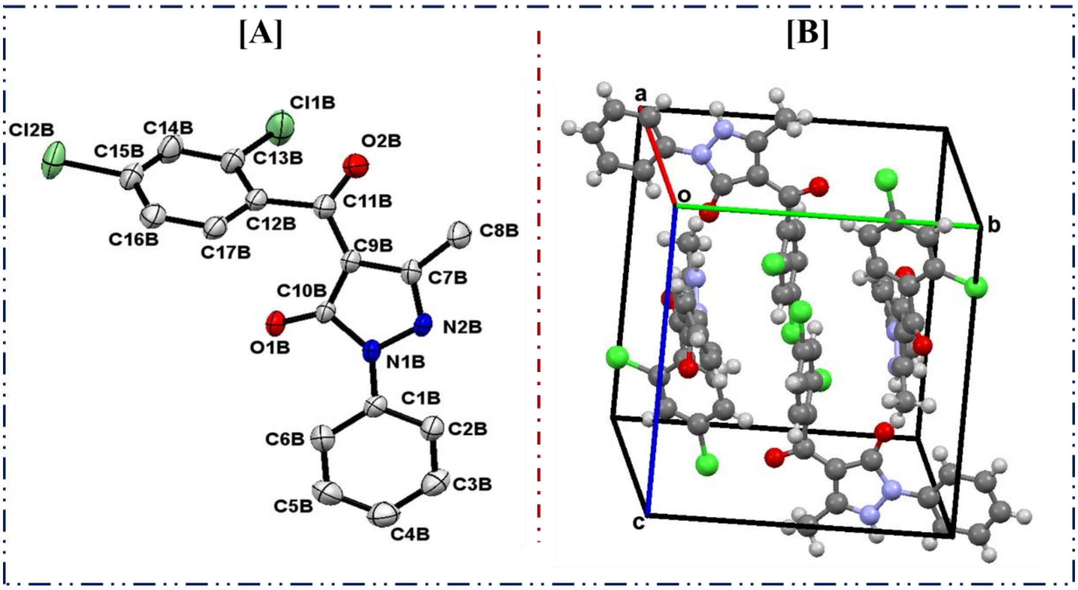

Fig.2.11. [A] Molecular structure (ORTEP view without hydrogen atoms) of HL^I ligand with anisotropic displacement ellipsoids drawn at 50%, [B] A perspective view of crystal packing plot of HL^I ligand along with a-axis

Table 2.2. Bond lengths & Bond angles parameters of HL^I ligand

Atoms	Bond lengths (Å)	Atoms	Bond lengths (Å)	Atoms	Bond angles (°)	Atoms	Bond angles (°)
C(1)-C(2)	1.373(4)	C(9)-C(10)	1.439(4)	C(1)-C(2)-C(6)	118.9(3)	N(1)-C(10)-C(9)	105.2(2)
C(1)-C(6)	1.376(4)	C(9)-C(11)	1.441(4)	C(2)-C(1)-N(1)	120.3(2)	O(1)-C(10)-C(9)	131.7(3)
C(1)-N(1)	1.417(4)	C(11)-C(12)	1.506(4)	C(6)-C(2)-N(1)	120.8(3)	O(1)-C(10)-N(1)	123.1(3)
C(2)-C(3)	1.378(5)	C(12)-C(13)	1.382(4)	C(1)-C(2)-C(3)	120.0(3)	O(2)-C(11)-C(9)	123.0(3)
C(3)-C(4)	1.365(5)	C(12)-C(17)	1.380(5)	C(4)-C(3)-C(2)	121.3(3)	O(2)-C(11)-C(12)	117.6(3)
C(4)-C(5)	1.354(5)	C(13)-C(14)	1.384(4)	C(6)-C(4)-C(3)	118.4(3)	C(12)-C(13)-Cl(1)	119.1(2)
C(5)-C(6)	1.378(5)	C(14)-C(15)	1.376(4)	C(4)-C(5)-C(6)	121.5(3)	C(14)-C(13)-Cl(1)	119.2(2)
C(7)-C(8)	1.489(4)	C(15)-C(16)	1.371(5)	C(1)-C(6)-C(5)	119.9(3)	C(14)-C(15)-Cl(2)	118.9(2)
C(7)-C(9)	1.389(4)	C(16)-C(17)	1.380(4)	C(9)-C(7)-C(8)	130.7(3)	C(16)-C(15)-Cl(2)	119.8(3)
C(7)-N(2)	1.323(4)	C(2)-H(2)	0.9300	N(2)-C(7)-C(8)	120.5(2)	C(10)-N(1)-C(1)	131.1(2)
N(1)-N(2)	1.380(3)	N(2)-H(2)	0.8600	N(2)-C(7)-C(9)	108.8(2)	N(2)-N(1)-C(1)	120.8(2)
C(13)-Cl(1)	1.731(3)	C(10)-O(1)	1.242(3)	C(7)-N(2)-H(2)	124.8	N(2)-N(1)-C(10)	108.1(2)
C(15)-Cl(2)	1.737(3)	C(11)-O(2)	1.221(4)	C(1)-C(6)-H(6)	120.1	N(1)-N(2)-H(2)	124.8

Table 2.3. HL^{I} ligand: Hydrogen bond parameters

D-H...A	d(D-H)	d(H...A)	d(D...A)	<(DHA)
N(2A)-H(2AA)-O(1B)	0.86	1.91	2.735(3)	160.3
N(2B)-H(2BA)-O(1A)	0.86	1.91	2.731(3)	159.7

Table 2.4. HL^{I} ligand: Symmetry transformation used to generate equivalent atoms

	Symmetry transformations
1	x,y,z
2	-x,-y,-z

(ii) Molecular crystal Structure of HL^{II} ligand

The HL^{II} ligand was recrystallized in the rectified spirit, yielding a yellow, transparent crystal in the enol form, as confirmed by single crystal diffraction analysis. The molecule adopts the '***P*2₁/n**' space group, characterized by '**Monoclinic symmetry**'. It includes a primitive lattice (*p*), a 2-fold screw axis (2_1) along the b-axis, and a glide plane (n), all of which contribute to the molecular packing and structural organization of the crystal. The characteristic C=O bond lengths of the ligand are 1.221(4) Å for the C(11)-O(2) of the 2,4-dichloro benzoyl group and 1.307(3) Å for the C(7)-O(1) of pyrazolone, both of which are close to the bond length of the C=O double bond [17]. In addition to this, The C(7)-N(1) bond, 1.343(3) Å, is close to the typical bond length observed for C=N double bonds [18]. The characteristic bond length of C(3)-Cl(1), C(17)-Cl(2) and C(15)-Cl(3) are found to be 1.741(3), 1.735(2) and 1.734(2), respectively. The HL^{II} ligand has two carbonyl groups which exhibit characteristic bond lengths of C=O, such as (1.307(3) Å) and (1.263(3) Å) for C7-O1 of Pyrazolone carbonyl and C11-O2 of 2,4- dichloro benzoyl carbonyl respectively. In addition, C9-N2 bond length is (1.307(3) Å) and (1.343(3) Å) for C7-N1. There is an intramolecular H-bonding between the oxygen of 2,4-dichloro benzoyl chloride and the H atom in the pyrazolone's OH group. The molecular crystal structure and crystal packing of the ligand are shown in **Fig.2.12.** The intramolecular H-bonding and symmetry elements of the HL^{II} ligand are shown in **Fig.2.13**. The significant bond lengths and bond angles parameters for the HL^{II} ligand are provided in **Table 2.5.** The relevant hydrogen bonding parameters and the associated symmetry transformations are presented in **Tables 2.6-2.7**, respectively.

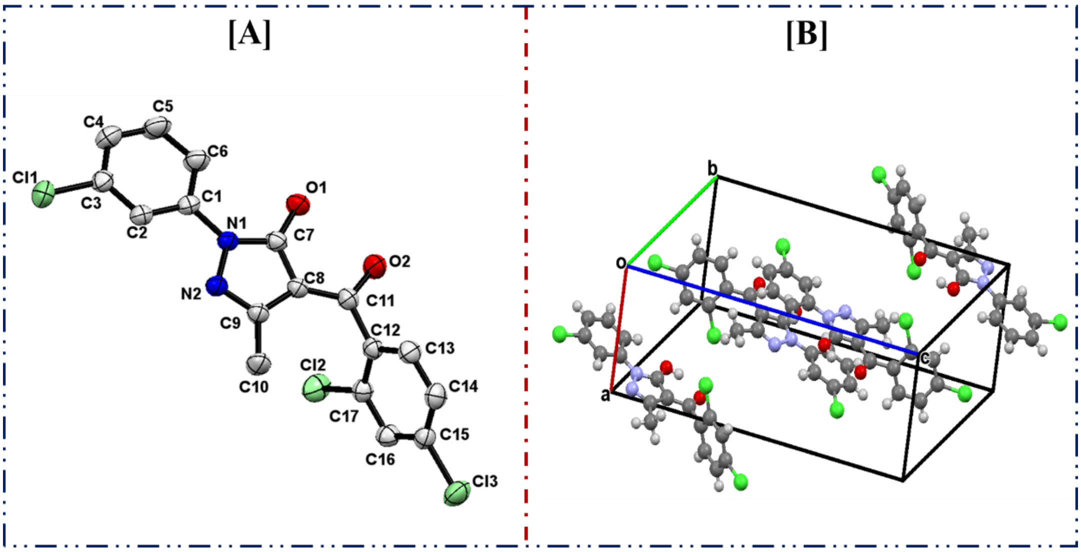

Fig.2.12. [A] Molecular structure (ORTEP view without hydrogen atoms) of HL^{II} ligand with anisotropic displacement ellipsoids drawn at 50 %, [B] A perspective view of crystal packing plot of HL^{II} ligand along with b-axis

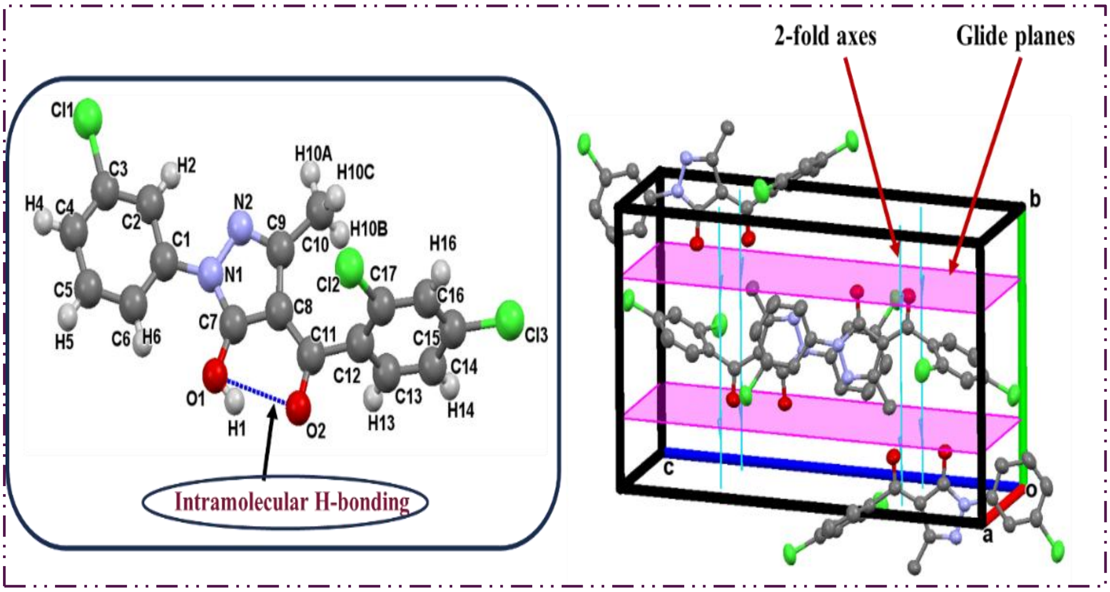

Fig.2.13. Intramolecular H-bonding between the hydrogen atom of a pyrazolone OH group and the oxygen atom of a benzoyl group and symmetry elements present in HL^{II} ligand

Table 2.5. Bond lengths & Bond angles parameters of HL^{II} ligand

Atoms	Bond lengths (Å)	Atoms	Bond lengths (Å)	Atoms	Bond angles (°)	Atoms	Bond angles (°)
C(1)-C(2)	1.382(3)	C(9)-C(10)	1.492(3)	C(1)-C(2)-C(6)	120.3(2)	C(7)-O(1)-H(1)	109.5
C(1)-C(6)	1.383(3)	C(14)-H(14)	0.9300	C(2)-C(1)-N(1)	118.2(2)	C(1)-C(2)-H(2)	120.6
C(1)-N(1)	1.419(3)	C(16)-H(16)	0.9300	C(6)-C(1)-N(1)	121.4(2)	C(3)-C(2)-H(2)	120.6
C(2)-C(3)	1.374(3)	O(1)-H(1)	0.8200	C(3)-C(2)-C(1)	118.8(2)	N(1)-C(7)-C(8)	107.8(19)
C(3)-C(4)	1.371(4)	C(2)-H(2)	0.9300	C(2)-C(3)-Cl(1)	118.7(2)	O(1)-C(7)-C(8)	127.6(2)
C(4)-C(5)	1.378(4)	C(9)-N(2)	1.307(3)	C(4)-C(3)-Cl(1)	118.7(19)	O(1)-C(7)-N(1)	124.6(2)
C(5)-C(6)	1.384(4)	N(1)-N(2)	1.400(2)	C(12)-C(17)-Cl(2)	119.2(18)	N(2)-C(9)-C(8)	111.4(19)
C(7)-C(8)	1.405(3)	C(11)-O(2)	1.263(3)	C(16)-C(17)-Cl(2)	122.2(2)	N(2)-C(9)-C(10)	119.5(2)
C(7)-N(1)	1.343(3)	C(3)-Cl(1)	1.741(3)	C(7)-N(1)-C(1)	131.1(19)	O(2)-C(11)-C(8)	120.1(2)
C(7)-O(1)	1.307(3)	C(17)-Cl(2)	1.735(2)	C(7)-N(1)-N(2)	110.2(17)	O(2)-C(11)-C(12)	116.9(2)
C(8)-C(9)	1.424(3)	C(15)-Cl(3)	1.734(2)	N(2)-N(1)-C(1)	118.7(17)	C(4)-C(5)-C(6)	121.7(3)
C(8)-C(11)	1.406(3)	C(16)-C(17)	1.383(3)	C(9)-N(2)-N(1)	106.3(17)	C(1)-C(6)-C(5)	119.0(3)

Table 2.6. HL^{II} ligand: Hydrogen bond parameters

D-H...A	d(D-H)	d(H...A)	d(D...A)	<(DHA)
O(1)-H(1)-O(2)	0.82	1.92	2.604(2)	140.6

Table 2.7. HL^{II} ligand: Symmetry transformation used to generate equivalent atoms

	Symmetry transformations
1	x,y,z
2	-x+1/2, y+1/2, -z+1/2
3	-x, -y, -z
4	x-1/2, -y-1/2, z-1/2

(iii) Molecular crystal Structure of HL^{III} ligand

The HL^{III} ligand has been recrystallized in the rectified spirit, yielding a pale yellow, needle-shaped crystal in the keto form, as confirmed by single crystal diffraction analysis. The ligand crystallizes in the "**Triclinic *P*-1**" space group. The characteristic C=O bond lengths of the ligand are 1.221(4) Å for the C(12)-O(2) of the 2,4-dichloro benzoyl group and 1.238(5) Å for the C(1)-O(1) of pyrazolone, both of which are close to the bond length of the C=O double bond [17]. In addition to this, The C(3)-N(2) bond, 1.328(6) Å, is close to the typical bond length observed for C=N double bonds [18]. The characteristic bond length 1.744(5) Å is observed for both C(14)-Cl(1) and C(16)-Cl(2). The molecular crystal structure and crystal packing of the HL^{III} ligand are shown in **Fig.2.14.** The significant bond lengths and bond angles parameters for the HL^{III} ligand are provided in **Table 2.8.** The relevant hydrogen bonding parameters and the associated symmetry transformations are presented in **Table 2.9** and **Table 2.10**, respectively.

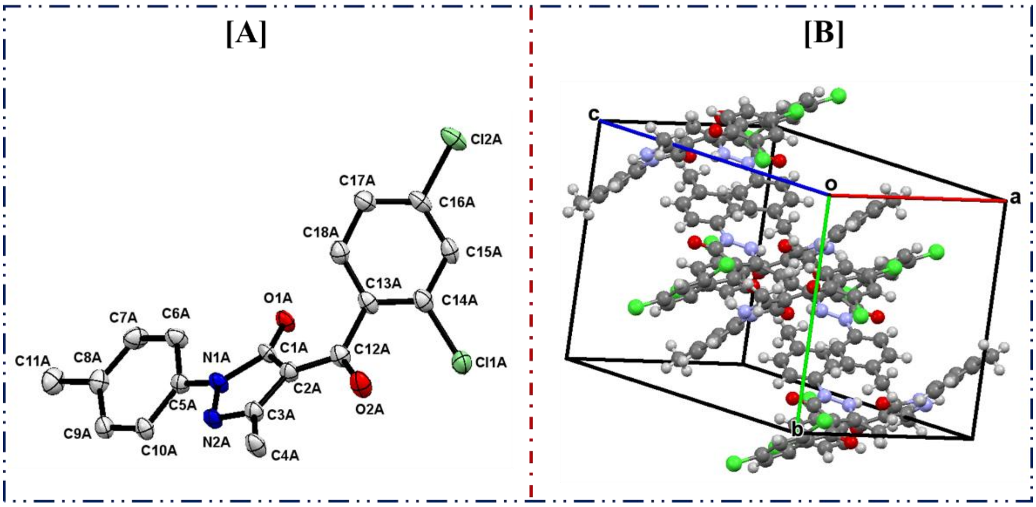

Fig.2.14. [A] Molecular structure (ORTEP view without hydrogen atoms) of HL^{I} ligand with anisotropic displacement ellipsoids drawn at 50 %, [B] A perspective view of crystal packing plot of HL^{III} ligand along with c-axis

Table 2.8. Bond lengths & Bond angles parameters of HL^{III} ligand

Atoms	Bond lengths (Å)	Atoms	Bond lengths (Å)	Atoms	Bond angles (°)	Atoms	Bond angles (°)
C(1)-C(2)	1.450(6)	C(5)-C(6)	1.389(6)	N(2)-N(1)-C(1)	109.0(4)	O(2)-C(12)-C(13)	118.8(4)
C(2)-C(3)	1.385(6)	C(6)-C(7)	1.394(7)	N(2)-N(1)-C(5)	120.0(4)	C(3)-C(2)-C(1)	107.6(4)
C(2)-C(12)	1.455(6)	C(7)-C(8)	1.384(7)	C(1)-N(1)-C(5)	130.8(4)	C(3)-C(2)-C(12)	124.4(4)
C(3)-C(4)	1.492(6)	C(8)-C(9)	1.391(7)	C(3)-N(2)-N(1)	109.7(4)	C(1)-C(2)-C(12)	127.8(4)
C(5)-C(10)	1.393(6)	C(8)-C(11)	1.507(7)	O(1)-C(1)-N(1)	123.2(4)	C(2)-C(3)-C(4)	131.3(4)
C(1)-O(1)	1.238(5)	C(9)-C(10)	1.393(7)	O(6)-C(1)-C(2)	132.4(4)	C(18)-C(13)-C(14)	117.8(4)
C(12)-O(2)	1.229(6)	C(12)-C(13)	1.500(6)	N(1)-C(1)-C(2)	104.5(4)	C(18)-C(13)-C(12)	119.8(4)
C(5)-N(1)	1.422(6)	C(13)-C(18)	1.386(7)	N(2)-C(3)-C(4)	119.6(4)	C(14)-C(13)-C(12)	122.2(4)
C(1)-N(1)	1.394(6)	C(7)-H(7)	0.9500	C(13)-C(14)-Cl(1)	120.5(4)	C(13)-C(14)-C(11)	120.5(4)
C(3)-N(2)	1.328(6)	C(10)-H(10)	0.9500	C(14)-C(15)-Cl(1)	117.5(4)	C(18)-C(17)-H(17)	121.1
N(1)-N(2)	1.385(5)	C(11)-H(11)	0.9800	C(15)-C(16)-Cl(2)	118.4(4)	C(16)-C(17)-H(17)	121.1

Table 2.9. HL^{III} ligand: Hydrogen bond parameters

D-H...A	d(D-H)	d(H...A)	d(D...A)	<(DHA)
N(2A)-H(2AA)-O(1B)	0.86(2)	1.87(2)	2.715(5)	170(6)
N(2B)-H(2BA)-O(1A)	0.86(2)	1.86(3)	2.704(5)	169(8)

Table 2.10. HL^{III} ligand: Symmetry transformation used to generate equivalent atoms

	Symmetry transformations
1	-x,-y+2,-z
2	-x,-y+1,-z+1
3	x+1,y,z
4	-x+1,-y+2,-z+1
5	-x+1,-y+1,-z+2

Table 2.11. Crystal data and details of refinement of ligands HL^I, HL^{II} and HL^{III}

CODE	HL^I ligand	HL^{II} ligand	HL^{III} ligand
CCDC number	2263829	2263580	2281709
Chemical formula	$C_{17}H_{12}Cl_2N_2O_2$	$C_{17}H_{11}Cl_3N_2O_2$	$C_{18}H_{14}Cl_2N_2O_2$
Formula weight	347.18	381.63	361.21
Crystal system	Triclinic	Monoclinic	Triclinic
Space group	P-1	$P2_1/n$	P-1
Volume	1568.39(7) Å^3	1668.22(5) Å^3	1664.99(11) Å^3
Temperature	298(2) K	298(2) K	100(2) K
Wavelength	1.54178 Å	1.54178 Å	1.54184 Å
Z	2	4	4
Density	1.470 Mg/m^3	1.519 Mg/m^3	1.441 Mg/m^3
Unit cell dimension	a = 11.5502(3) Å	a = 7.44180(10) Å	a = 12.1180(3) Å
	b = 11.5976(3) Å	b = 11.3843(2) Å	b = 12.3703(4) Å
	c = 12.1851(3) Å	c= 19.8633(4) Å	c = 12.5275(5) Å
	α= 93.586(2)°	α,γ = 90°	α= 62.609(4)°
	β= 90.901(2)°	β= 97.5520(10)°	β= 87.115(3)°
	γ= 105.568(2)°		γ= 87.752(3)°
F (0 0 0)	712	776	744
Theta range	66.414 to 3.975°	66.706 to 4.487°	3.653 to 79.009°
Absorption Correction	Multi-scan	Multi-scan	Semi-empirical from equivalents
Absorption coefficient	3.818 mm^{-1}	5.086 mm^{-1}	3.617 mm^{-1}
Index ranges	-13<=h<=13	-7<=h<=8	-10<=h<=15
	-13<=k<=13	-13<=k<=9	-16<=k<=16
	-14<=l<=14	-23<=l<=22	-26<=l<=25
Independent reflections	6526 [R_{int} = 0.0659]	2954 [R_{int} = 0.0399]	1370 [R_{int} = 0.0643]
Goodness-of-fit on F^2	1.058	1.047	1.196
Final R indices	R_1 = 0.0771	R_1 = 0.0510	R_1 = 0 .1336
[I>2sigma(I)]	wR2 = 0.0490	wR2 = 0.1065	wR2 = 0.4069
Data/restraints/parameters	5486/0/417	2954/0/219	1370/4/878

2.3.4 DFT based computational analysis

To investigate and correlate the chemical and physical properties of the synthesized ligands HL^I, HL^{II} and HL^{III}, Density Functional Theory (DFT) was employed. The theoretical calculations were performed on isolated molecules (gas phase), whereas the experimental results were obtained in the solid state [19]. The initial step in the computational analysis was to determine the optimized geometry of each compound. The molecular structures of these compounds in their ground state were computed using the B3LYP functional with the 6-31G basis set [20]. The B3LYP approach and GaussView 6.0 software were used for processing the input files [21][22]. The optimized geometries of the HL^I, HL^{II} and HL^{III} ligands yielded electronic energy (optimization energy) values of −49.934, −62.440 and −51.004 keV, respectively. The more negative optimization energy of the HL^{II} ligand implies greater stability. The optimized geometries of the ligands are depicted in **Fig.2.15.**

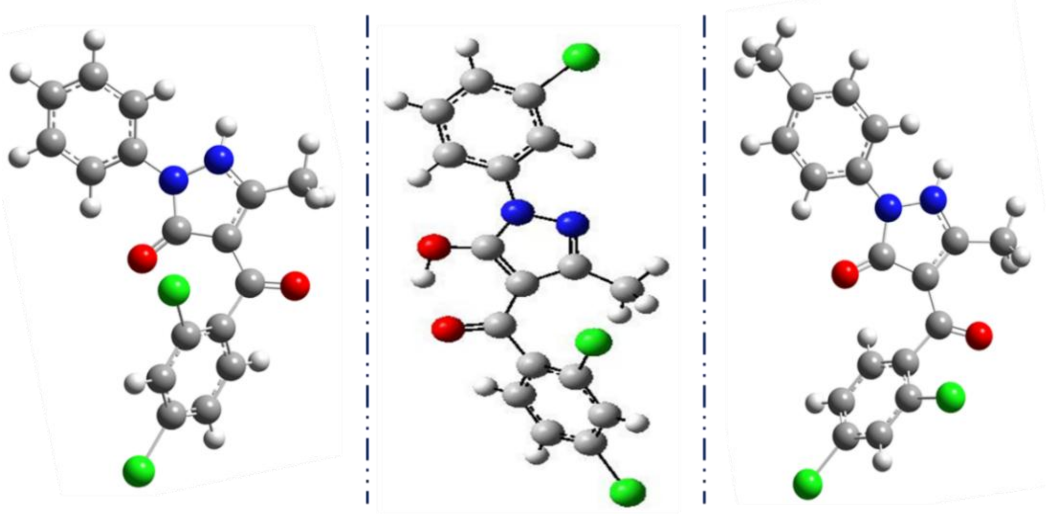

HL^I ligand HL^{II} ligand HL^{III} ligand

Fig.2.15. DFT optimized geometries of HL^I, HL^{II} and HL^{III} ligands

2.3.4.1 A Frontier molecular orbital energy (HOMO-LUMO) analysis

The HOMO-LUMO energies play a key role in understanding the various chemical interactions. The HOMO-LUMO gap provides insights into the molecule's characteristics, such as its hardness, softness and reactivity. The negative energy values demonstrate the stability of the molecule [23]. In addition to reflecting chemical stability, HOMO-LUMO orbitals are crucial for determining the electrical transport properties of the molecules [19]. The charge transfer interactions within the molecule are clarified by the electron-accepting ability of the electron-acceptor group, as demonstrated by the decrease in the HOMO-LUMO energy gap. The energy gap between the HOMO and LUMO levels plays a key role in determining a molecule's kinetic stability, reactivity, optical polarizability, and chemical hardness or softness. By examining the composition of these molecular orbitals (HOMO and LUMO), it is possible to estimate the molecular properties that affect the selectivity and reactivity of the compounds. These properties can be approximated using Koopman's theorem, which links the HOMO and LUMO energies to ionization energy and electron affinity [24]. It is evident from the computed HOMO and LUMO energies that charge transfer takes place within the molecule [20].

The six Frontier Molecular Orbitals (FMOs) of the ligands HL^{I}, HL^{II} and HL^{III} are depicted in **Figs.2.16-2.18,** respectively. The HOMO-LUMO energy values of three ligands are explained in **Table 2.12.** The energy difference between the LUMO and HOMO orbitals demonstrates the molecular bond's stability. A high HOMO-LUMO gap suggests that the molecule is stable and has little chemical reactivity. The fact that all of the HOMOs have paired electrons clarifies the diamagnetic behaviour of all three ligands. The energy gap (ΔE) values for HL^{I}, HL^{II} and HL^{III} ligands are sequentially 4.242 eV, 4.438 eV and 4.246 eV. The global parameters of ligands are given in **Table 2.13,** which provides an extensive understanding of the ligand's properties. All the refinement parameters of all three ligands are listed in **Table 2.11.**

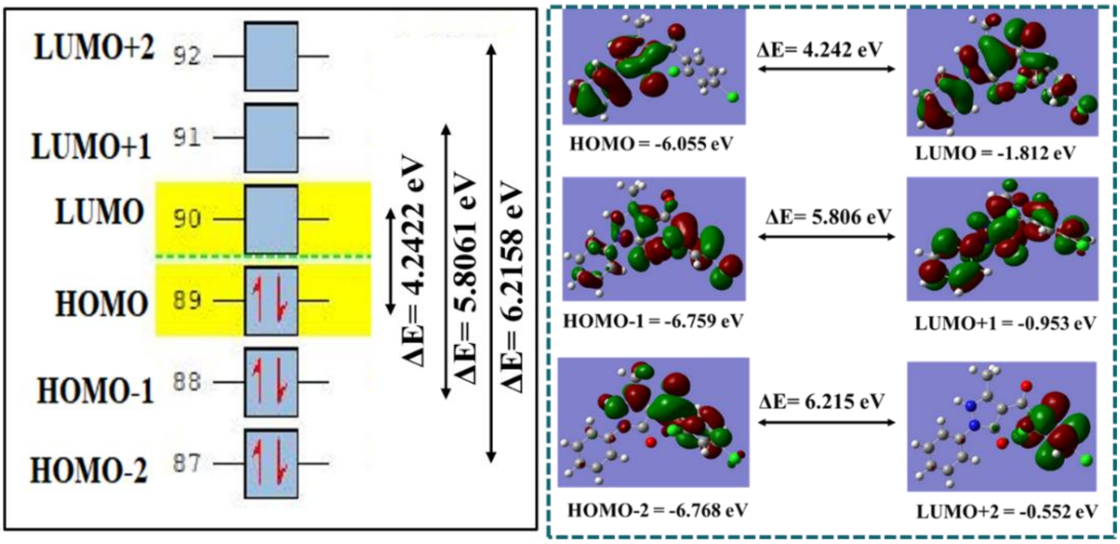

Fig.2.16. HOMO-LUMO molecular orbital energy diagram of HL^{I} ligand

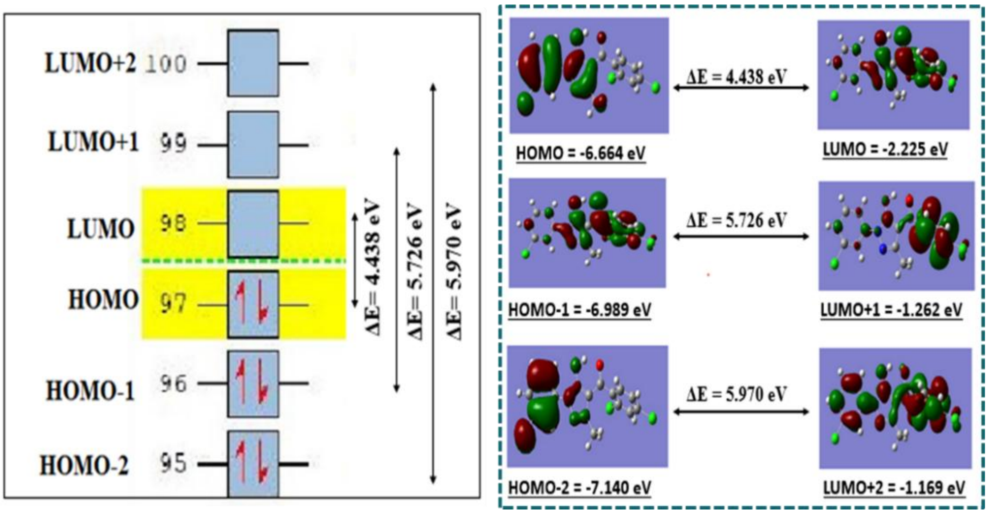

Fig.2.17. HOMO-LUMO molecular orbital energy diagram of HL^{II} ligand

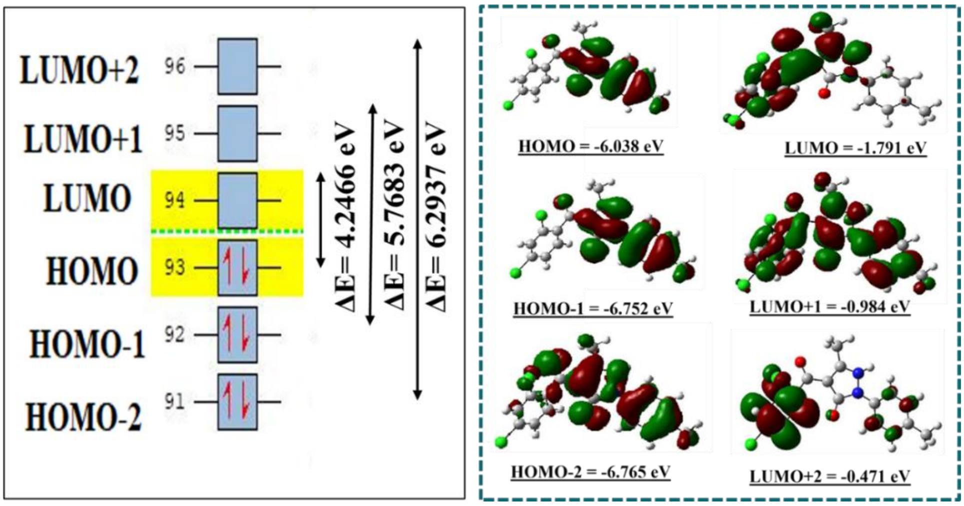

Fig.2.18. HOMO-LUMO molecular orbital energy diagram of HL^{III} ligand

Table 2.12. HOMO-LUMO energy values of ligands HL^{I}, HL^{II} and HL^{III}

Levels	Molecular orbital energy (eV)		
	HL^{I} Ligand	HL^{II} Ligand	HL^{III} Ligand
HOMO	-6.055	-6.664	-6.038
LUMO	-1.812	-2.225	-1.791
HOMO-1	-6.759	-6.989	-6.752
LUMO+1	-0.953	-1.262	-0.984
HOMO-2	-6.768	-7.140	-6.765
LUMO+2	-0.552	-1.169	-0.471

Table 2.13. Global parameters of ligands HL^{I}, HL^{II} and HL^{III}

Properties	Mathematical formulas	HL^{I} Ligand	HL^{II} ligand	HL^{III} ligand
E_{HOMO}	E_{HOMO}	-6.055	-6.664	-6.038
E_{LUMO}	E_{LUMO}	-1.812	-2.225	-1.791
ΔE	$\Delta E = E_{LUMO} - E_{HOMO}$	4.242	4.438	4.246
Ionization potential (IP)	$IP = -E_{HOMO}$	6.055	6.664	6.038
Chemical Potential (μ)	$\mu = 1/2\ (E_{HOMO} + E_{LUMO})$	-3.933	-4.444	-3.914
Electron affinity (EA)	$EA = -E_{LUMO}$	1.812	2.225	1.791
Electronegativity (EN)	$EN = -1/2\ (E_{HOMO}+E_{LUMO})$	3.933	4.444	3.914
Global Hardness (η)	$\eta = -\ 1/2\ (E_{HOMO}-E_{LUMO})$	2.121	2.219	2.123
Softness (S)	$S = 1/2\eta$	0.235	0.225	0.235
Electrophilicity index (ω)	$\omega = \mu^2/2\eta$	3.646	4.450	3.607

The optimized geometries of all three ligands were used as the input for the vibrational frequency analysis. After achieving convergence, harmonic vibrational frequencies were computed at the same theoretical level to confirm that the stationary point exhibited no imaginary frequencies. When the theoretical values are in close agreement with the experimental spectra, the considerations discussed in the section on FTIR spectroscopic analysis become extremely important. Theoretical IR frequencies were calculated through a DFT study. The key theoretical vibrations are shown with the actual FTIR spectrum values in **Table 2.14**. The DFT-optimized FTIR spectra of all three ligands are displayed in **Figs.2.19–2.21**. Theoretical infrared (IR) frequencies tend to be higher than experimental ones because computational IR calculations typically model molecules in an isolated gas-phase state without considering external factors like hydrogen bonding or intermolecular interactions, which are present in real-world conditions. These practical factors, along with non-ideal vibrational behaviour (anharmonicity), cause a reduction in the IR frequencies observed during experimental measurements. Furthermore, computational methods often simplify the description of molecular vibrations by assuming harmonic motion, which results in an overestimation of frequencies compared to actual experimental values. These differences stem from the approximations and environmental effects that theoretical models do not fully incorporate.

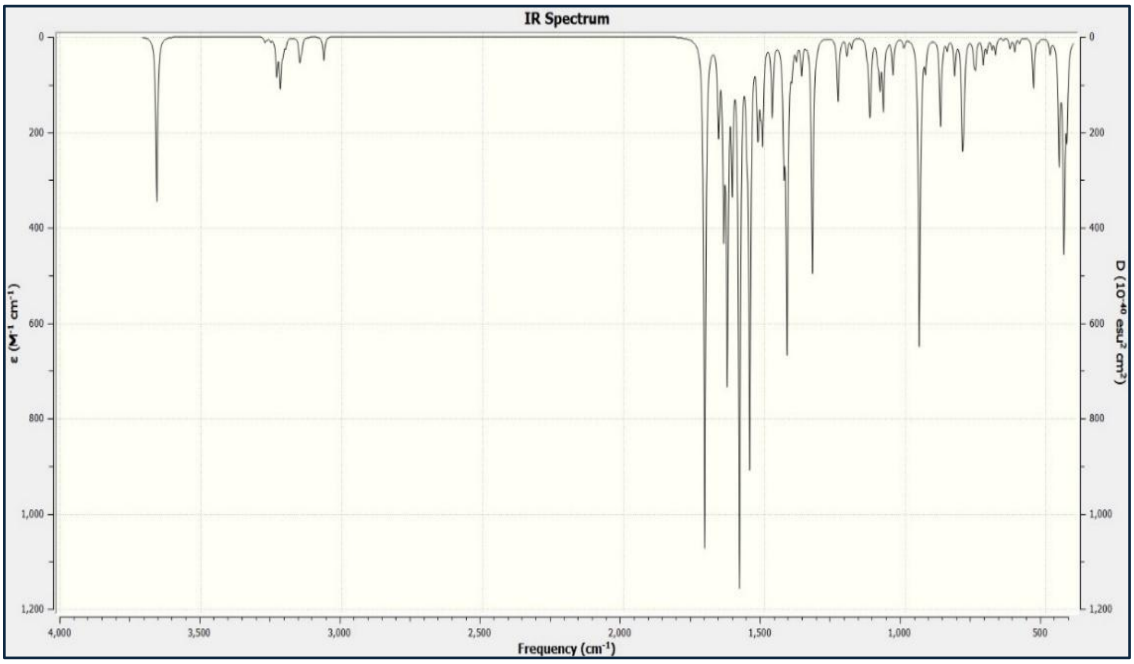

Fig.2.19. FTIR spectrum of HL^{I} ligand through DFT computational analysis

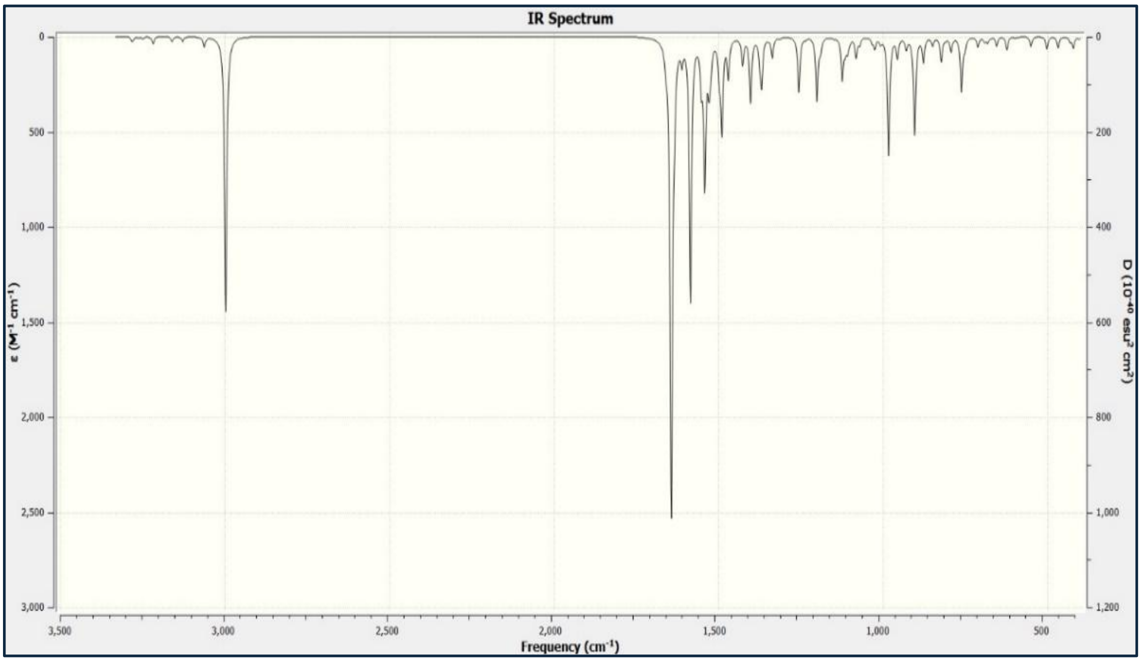

Fig.2.20. FTIR spectrum of HL^{II} ligand through DFT computational analysis

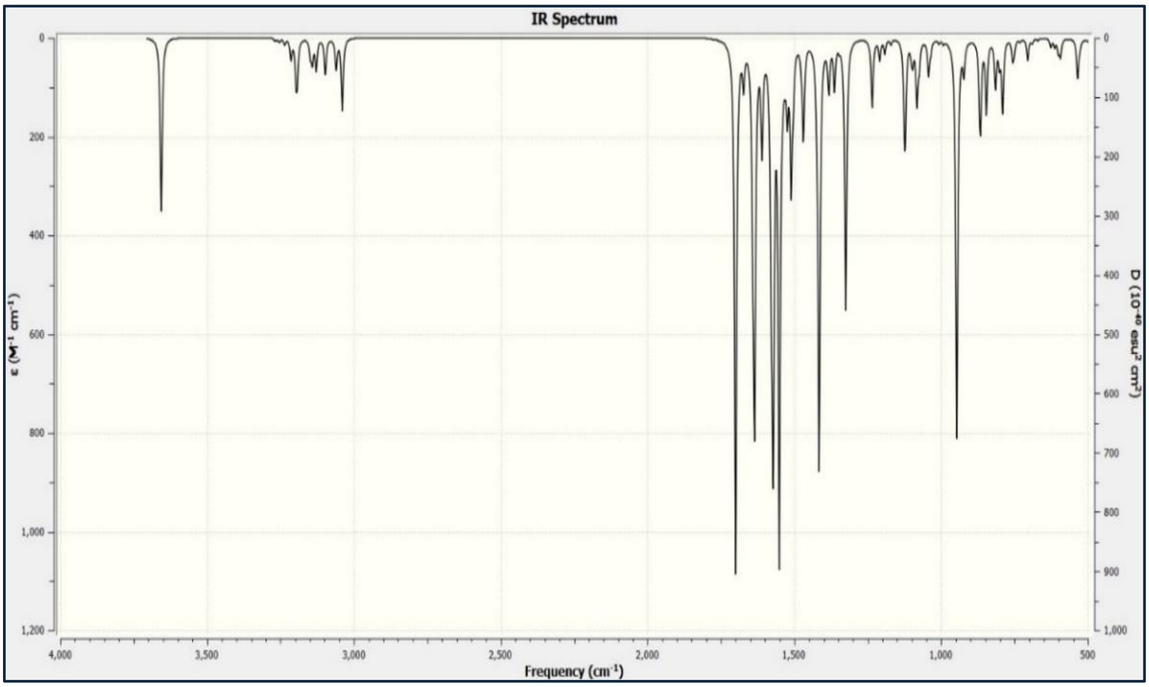

Fig.2.21. FTIR spectrum of HL^{III} ligand through DFT computational analysis

Table 2.14. Comparison of theoretical and practical FTIR vibrational data of HL^{I}, HL^{II} and HL^{III} ligands

IR Frequencies (cm^{-1})	HL^{I} ligand		HL^{II} ligand		HL^{III} ligand	
	TH	PR	TH	PR	TH	PR
ν(C=O) of 2,4- dichloro benzoyl	1629	1587	1585	1550	1640	1585
ν(C=O) of Pyrazolone	1709	1627	1640	1594	1700	1668
Cyclic ν(C=N)	1549	1515	1551	1482	1450	1472
C–H in-plane deformation	1400	1394	1123	1100	1300	1253

The structural consistency was verified by comparing bond angles and distances between the DFT-optimized structures and those obtained through X-ray crystallography. While the experimental data were collected in the solid state, the theoretical calculations were performed on isolated molecules in the gas phase. The optimized bond lengths and angles were slightly larger than the experimental values. Additionally, the theoretical IR frequencies are higher than the observed FT-IR frequencies, as illustrated in **Table 2.15.** Overall, there is good agreement between the optimized geometry and the experimental results.

Table 2.15. Comparison of bond lengths (Å) and bond angles (°) of HL^{I}, HL^{II} and HL^{III} ligands

Atoms	Practical bond length (Å)	Theoretical bond length (Å)	Atoms	Practical bond angles (°)	Theoretical bond angles (°)
HL^{I} ligand					
C(1)-N(1)	1.417(4)	1.416	C(2)-C(1)-N(1)	120.3(2)	120.29
C(7)-N(20	1.323(4)	1.361	C(6)-C(1)-N(1)	120.8(3)	119.55
C(10)-N(1)	1.399(3)	1.426	N(2)-C(7)-C(8)	120.5(2)	120.71
C(10)-O(1)	1.242(3)	1.248	N(2)-C(7)-C(9)	108.8(2)	108.65
C(11)-O(2)	1.221(4)	1.259	N(1)-C(9)-C(10)	105.2(2)	104.64
N(1)-N(2)	1.380(3)	1.402	O(1)-C(10)-C(9)	131.7(3)	131.57
Cl(1)-C(13)	1.731(3)	1.852	O(1)-C(10)-N(1)	123.1(3)	123.77
Cl(2)-C(15)	1.737(3)	1.856	O(2)-C(11)-C(12)	117.6(3)	118.26
C(1)-C(2)	1.373(4)	1.420	N(2)-N(1)-C(1)	120.8(2)	121.01
C(8)-C(7)	1.489(4)	1.491	N(2)-N(1)-C(10)	108.1(2)	108.23
HL^{II} ligand					
C(3)-Cl(1)	1.741(3)	1.830	C(6)-C(1)-N(1)	121.4(2)	121.36
C(17)-Cl(2)	1.735(2)	1.826	C(8)-C(7)-N(1)	107.81(19)	108.37
C(15)-Cl(3)	1.734(2)	1.825	C(9)-C(10)-N(2)	119.5(2)	119.16
C(1)-N(1)	1.419(3)	1.422	C(8)-C(9)-N(2)	111.42(19)	110.91
C(7)-N(2)	1.343(3)	1.354	C(2)-C(1)-N(1)	118.2(2)	117.90
C(9)-N(2)	1.307(3)	1.332	O(1)-C(7)-C(8)	127.6(2)	126.76
N(1)-N(2)	1.400(2)	1.424	O(1)-C(7)-N(1)	124.6(6)	124.85
C(7)-O(1)	1.307(3)	1.343	C(4)-C(3)-Cl(1)	118.7(19)	124.32
C(11)-O(2)	1.263(3)	1.279	C(16)-C(17)-Cl(2)	122.2(2)	136.34
C(9)-C(10)	1.492(3)	1.494	N(2)-N(1)-C(1)	118.7(17)	125.35
HL^{III} ligand					
C(1)-O(1)	1.238(5)	1.250	O(1)-C(1)-N(1)	123.2(4)	123.19
C(12)-O(2)	1.229(6)	1.257	C(6)-C(5)-N(1)	120.3(4)	119.77
C(14)-Cl(1)	1.744(5)	1.823	N(1)-C(1)-C(2)	104.5(4)	104.73
C(16)-Cl(2)	1.744(5)	1.823	N(2)-N(1)-C(5)	120.4(5)	120.93
N(1)-N(2)	1.385(5)	1.400	C(3)-N(2)-N(1)	109.7(4)	110.08
C(5)-N(1)	1.422(6)	1.510	N(2)-C(3)-C(4)	119.6(4)	120.44
C(1)-N(1)	1.394(6)	1.425	C(10)-C(5)-N(1)	119.6(4)	120.49
C(3)-N(2)	1.328(6)	1.359	C(17)-C(16)-Cl(2)	119.5(6)	119.32
C(1)-C(2)	1.450(6)	1.490	C(15)-C(16)-Cl(2)	118.4(4)	118.68

2.3.5 Hirshfeld surface area analysis

After F.L. Hirshfeld, whose "stockholder partitioning" approach for designating atoms in molecules suggested to us an extension to characterising a molecule in a crystal, Hirshfeld surfaces were named in his honour. The Hirshfeld surface was created in an effort to specify the area a molecule takes up in a crystal in order to divide the electron density of crystals into snippets of molecules [25]. To gain further insight into the interactions between molecules in crystal formations, Hirshfeld surfaces analysis has been utilised. This work has given a detailed account of the molecule's near environment [26]. In this investigation, the donor-acceptor contact sites, and intermolecular interactions were visualised and examined using the Crystal Explorer 17.5 software. HS has been created over dnorm, de, di, shape index, curvedness and fragment patch. On the dnorm surface, blue areas represent regions where intermolecular distances are shorter than the van der Waals contact distance, indicating stronger interactions or possible overlaps. White areas signify distances close to the van der Waals contact distance, suggesting weaker interactions.

Bright red spots on the dnorm Hirshfeld surface emphasize strong hydrogen bonding interactions [27]. Curvedness, derived from the RMS curvature, shows that flat regions on the surface exhibit low curvedness, whereas areas with sharp features display high curvedness [28][29]. The shape index is highly sensitive to minor variations. Concave regions of the shape index are depicted by yellow-orange triangles, indicating atoms involved in $\pi\cdots\pi$ stacking interactions [27]. The red and blue triangles represent shorter, non-covalent interactions. The patches on the fragment patch depict various fragments of neighbouring molecules that are in close proximity to different areas of the surface. These colour-coded patches help identify regions where specific types of interactions, such as hydrogen bonding or van der Waals forces, occur. Using 2D fingerprint plots, non-covalent interactions that contribute to the stability of crystal packing can be analyzed quantitatively. A 2D fingerprint plot graphically summarizes the intermolecular interactions on the Hirshfeld surface. This plot is typically a two-dimensional histogram displaying the distances between atoms inside and outside the surface. The interaction between an atom in one molecule and neighbouring atoms in the ligand illustrates another example of efficient molecular packing [30]. Blue areas indicate a low frequency of contacts, while white areas show an absence of contacts or significant interactions. **Figs.2.22-2.27** display the 3D Hirshfeld surfaces and fingerprint plot of ligands HL^{I}, HL^{II} and HL^{III}.

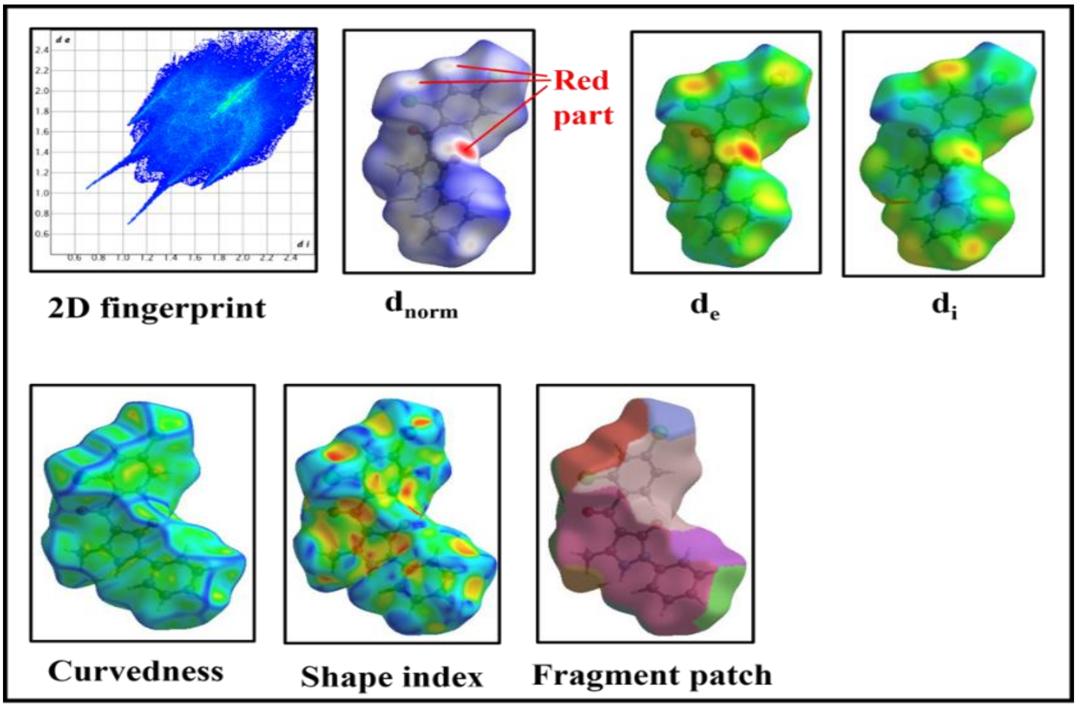

Fig.2.22 The molecular Hirshfield (full FP diagram, dnorm, di, de, Curvedness, Shape index, and fragment patch) of HL^{I} ligand

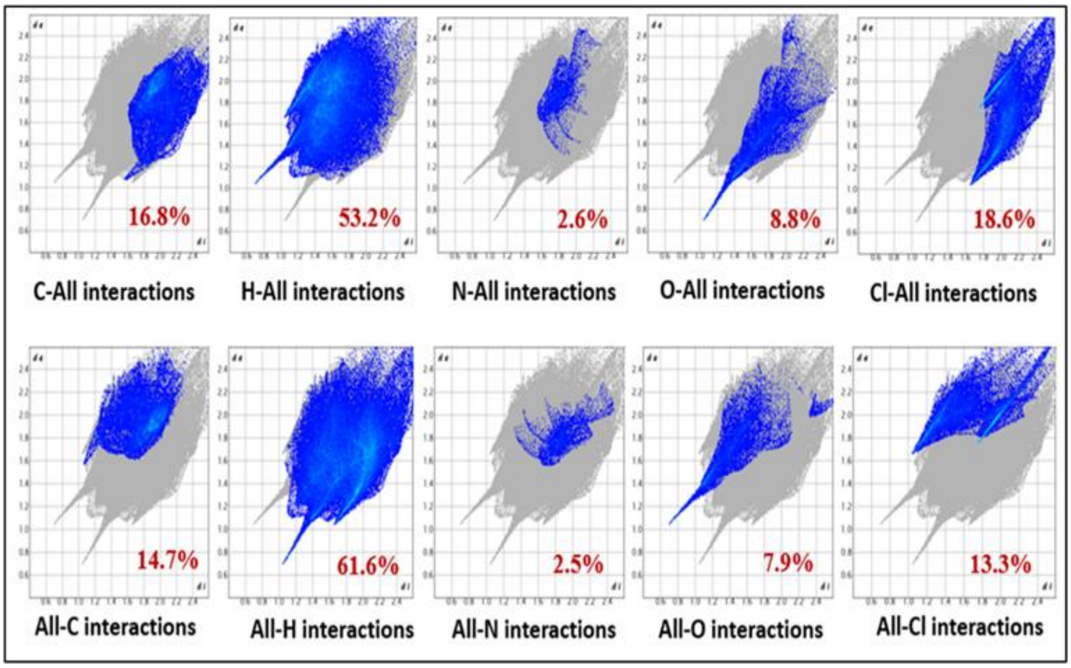

Fig.2.23. 2D fingerprint plot for HL^{I} ligand

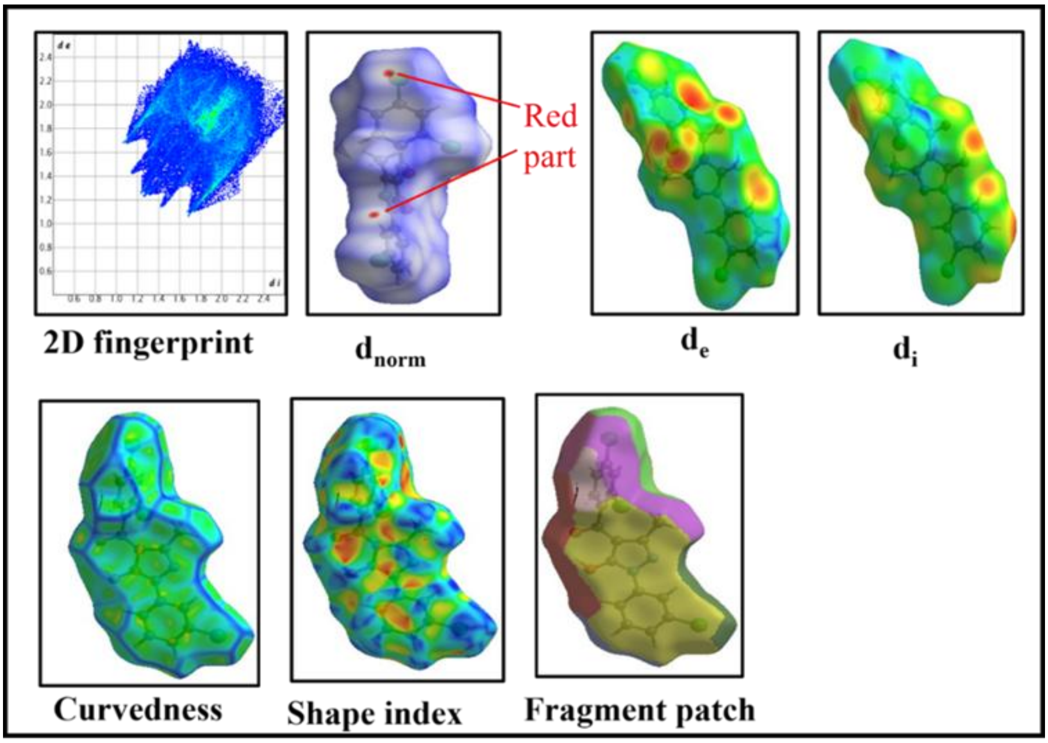

Fig.2.24. The molecular Hirshfeld (full FP diagram, dnorm, di, de, Curvedness, Shape index, and fragment patch) of HL^{II} ligand

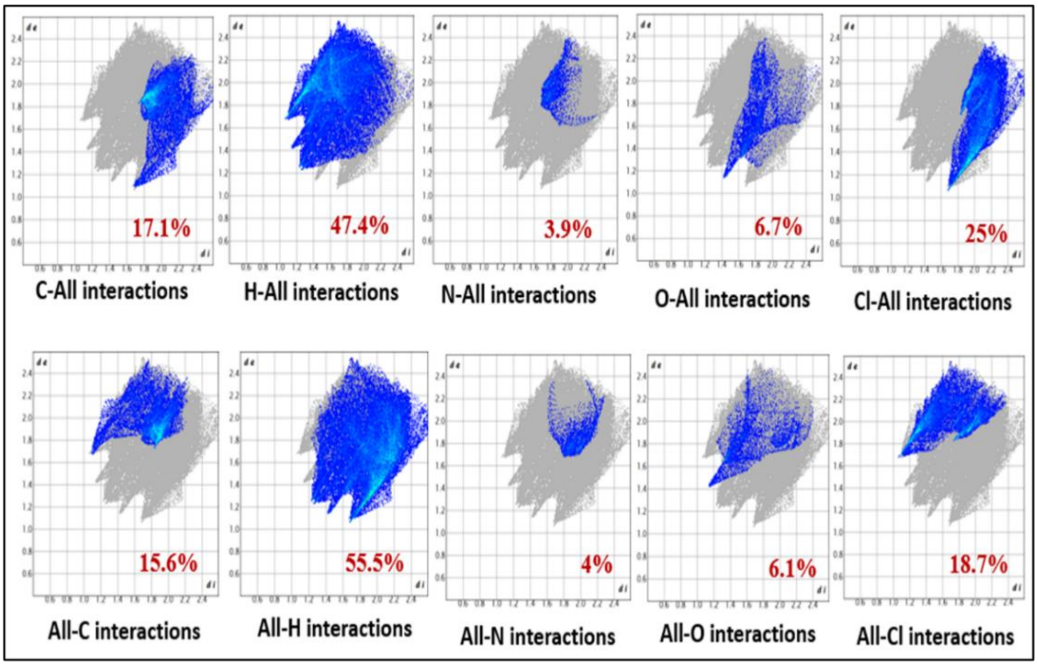

Fig.2.25. 2D fingerprint plot for HL^{II} ligand

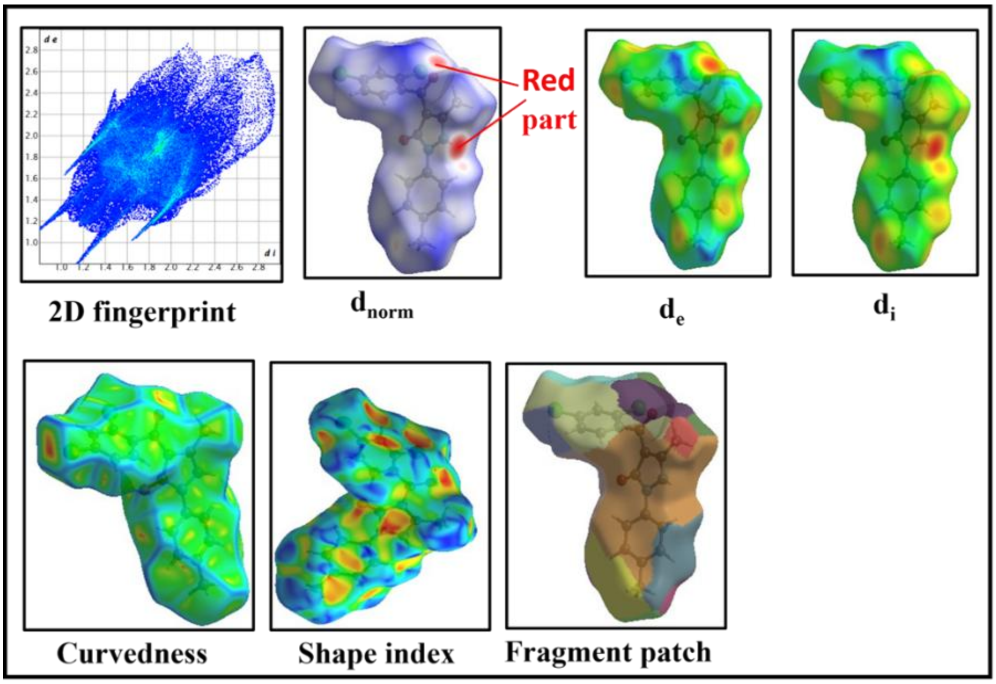

Fig.2.26. The molecular Hirshfield (full FP diagram, dnorm, di, de, Curvedness, Shape index, and fragment patch) of HL^{III} ligand

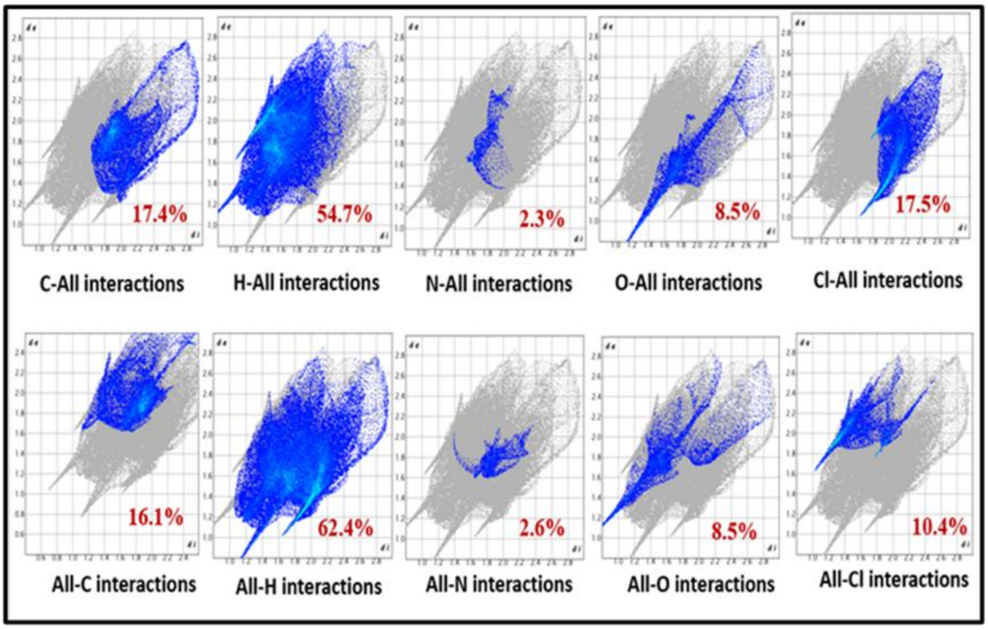

Fig.2.27. 2D fingerprint plot for HL^{III} ligand

The packing potential of the ligands can be assessed using percentage statistics for interactions between all atoms and specific atoms. This data provides insight into the likelihood of packing within the ligands. H-atoms have shown significant interactions across all ligands. Interactions involving C-All, O-All, N-All, H-All, and Cl-All, as well as inside-to-outside atom interactions for all three synthesized ligands, are depicted in **Figs.2.28-2.30**.

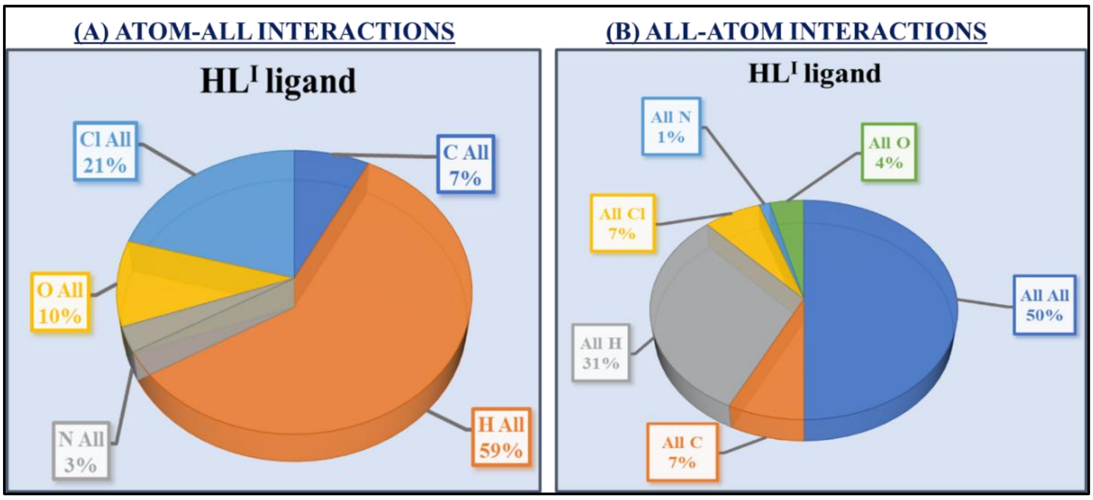

Fig.2.28. Graphical presentation of percentage interactions between atoms of HL^{I} ligand

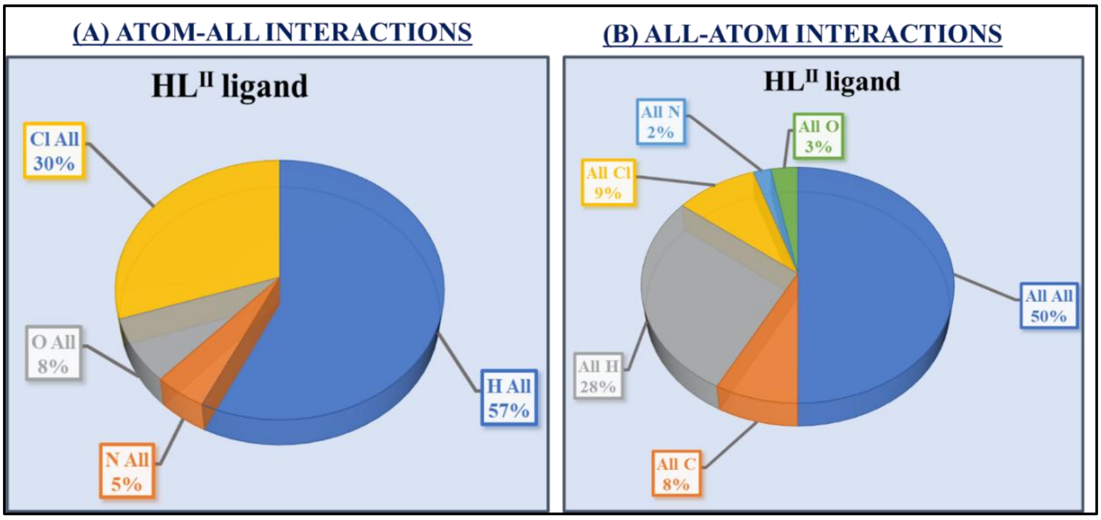

Fig.2.29. Graphical presentation of percentage interactions between atoms of HL^{II} ligand

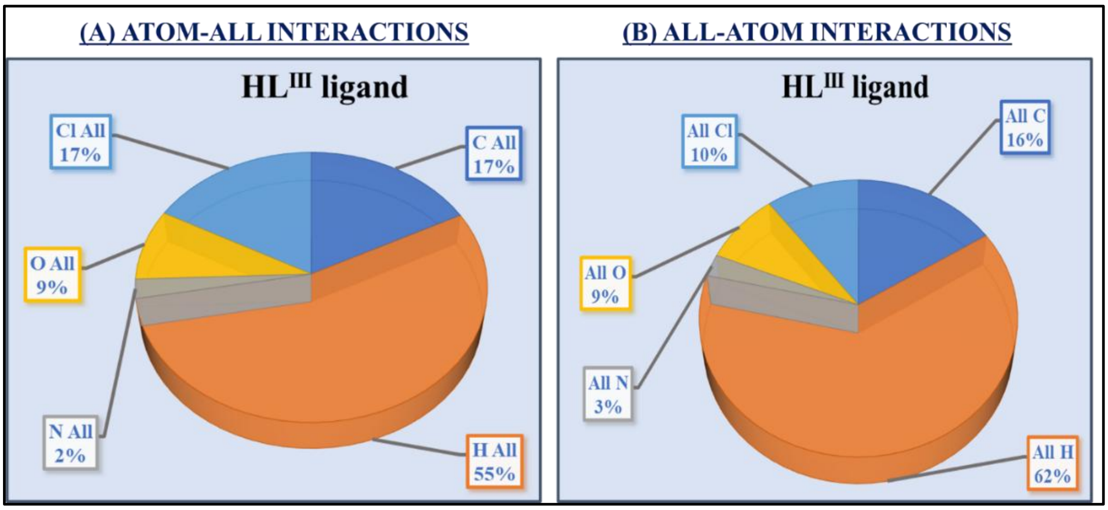

Fig.2.30. Graphical presentation of percentage interactions between atoms of HL^{III} ligand

A Hirshfeld surface (HS) analysis was conducted to find intermolecular interactions within the crystal lattice. Energy calculations were carried out for a 3.8 Å cluster surrounding the chosen HS of ligands HL^I, HL^{II} and HL^{III} as a first phase of the HS investigation to determine exact energy parameters and crystal strength. The fast [HF/3-21G] model of the Crystal Explorer 17.5 program was utilised to calculate the interaction energy data [31][32]. **Tables 2.16, 2.18** and **2.20** outline the interaction energies (in kJ mol^{-1}) between ligands HL^I, HL^{II} and HL^{III} and their surrounding molecules in that order. In Hirshfeld surface analysis, especially within the energy framework approach, scale factors are used to adjust benchmark energy models, ensuring that the calculated interaction energies between molecules in a crystal more accurately represent the actual physical interactions. These scale factors fine-tune and correct the interaction energies, making the computational results align more closely with experimental data or higher-level theoretical predictions. The scale factors for benchmarked energy models of HL^I, HL^{II} and HL^{III} ligands are listed in **Tables 2.17, 2.19** and **2.21**, respectively.

Four fundamental components are displayed along with the interaction energies (in kJ mol^{-1}) of a chosen molecule with its neighbouring molecules: the electrostatic component (Eele), the polarisation component (Epol), the dispersion component (Edis), and the repulsion component (Erep). Molecules with identical shades represent pairs of molecules, and N represents the number of molecules in each pair. R is the distance ratio (in Å) between the centroids, and the symbol represents the rotational operators between the pair and the centre molecule [33]. A fifth fundamental component (Lattice energy) was found by applying the following formula: lattice energy was estimated, which gives information about the strength of the bonds between the ligands. $\mathbf{E_{Lat.} = 0.5\ (N\ x\ E_{total})}$

The energy framework diagrams with a tube size of 70 and a cut-off (Threshold) energy of 5, 6 and 6 kJ mol^{-1} for HL^I, HL^{II} and HL^{III} ligands are respectively depicted in **Figs.2.31-2.33.** The diagrams highlight the Coulomb energy, Total energy, Dispersion energy and Total energy (annotated). The anisotropy of the molecule and interatomic interaction topology is shown graphically in these energy framework diagrams. The colours red or yellow, blue and green cylinders stand for coulomb energy, total energy and dispersion energy. A connection between the cylinders depicts the interactions between the centroids of molecules.

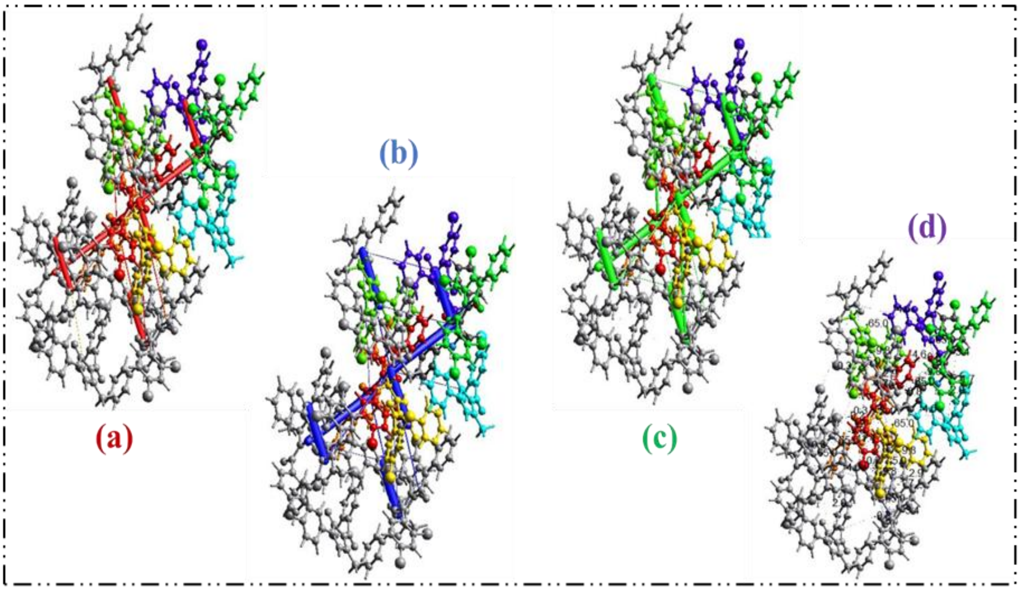

Fig.2.31. Energy frameworks in HL^{I} ligand based on (a) Coulomb energy, (b) Total energy, (c) Dispersion energy and (d) Total energy (annotated)

Table 2.16. The interaction energies (in kJ/mol) between the HL^{I} ligand molecule and surrounding molecules

	N	Symop	R	Electron Density	E_{ele}	E_{pol}	E_{dis}	E_{rep}	E_{total}	E_{Lat}
🟥	1	-x, -y, -z	8.33	HF/3-21G	-26.7	-8.1	-61.9	28.7	-65.0	-32.5
🟧	1	x, y, z	11.60	HF/3-21G	-3.2	-3.5	-8.5	4.2	-9.8	-4.9
🟨	1	-	14.92	HF/3-21G	11.6	-0.1	-3.2	0.0	8.8	4.4
🟩	0	-	9.69	HF/3-21G	0.4	-0.0	-0.1	0.0	0.3	0.0
🟩	1	-	6.75	HF/3-21G	-0.4	-0.8	-4.1	0.0	-4.6	-2.3
🟩	1	-x, -y, -z	8.58	HF/3-21G	0.0	-5.3	0.0	0.0	-3.4	-1.7
🟩	0	x, y, z	12.19	HF/3-21G	-5.5	-0.8	-4.1	0.0	-9.8	0.0
🟦	1	-	6.36	HF/3-21G	3.1	-0.1	-0.1	0.0	2.9	1.45
🟦	0	-	7.48	HF/3-21G	-0.1	-0.0	-0.1	0.0	-0.2	0.0
🟦	0	-x, -y, -z	9.88	HF/3-21G	-4.8	-1.2	-18.9	21.9	-5.0	0.0
🟪	1	-	6.45	HF/3-21G	-26.7	-8.1	-61.9	28.7	-65.0	-32.5
🟪	0	-	8.92	HF/3-21G	-0.9	-0.1	-0.8	0.0	-1.7	0.0
🟪	0	-	14.92	HF/3-21G	-0.3	-0.0	-0.0	0.0	-0.3	0.0

Table 2.17. Scale factors for benchmarked energy models of HL^{I} ligand

Energy Model	K_{ele}	K_{pol}	K_{disp}	K_{rep}
CE-HF ... HF/3-21G electron densities	1.019	0.651	0.901	0.811

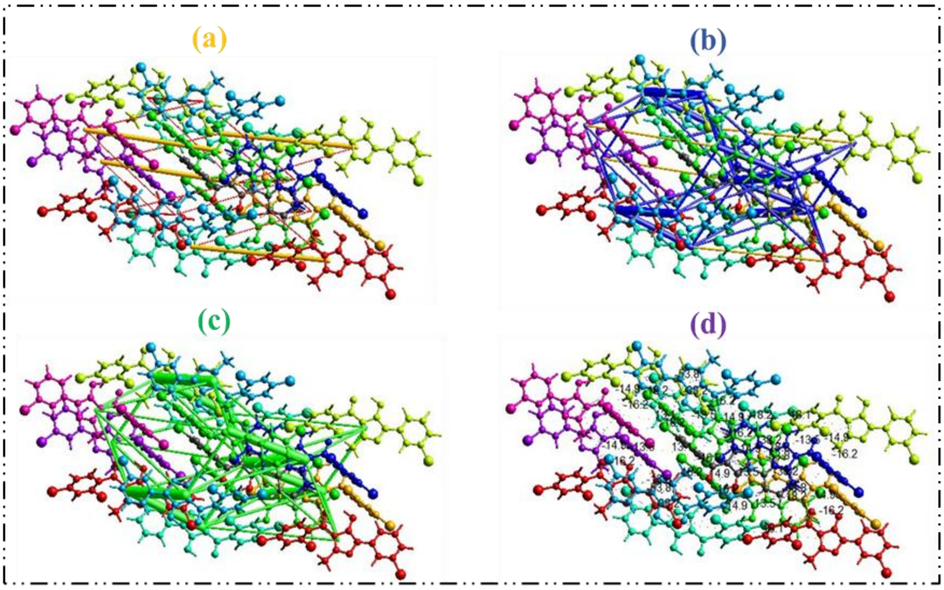

Fig.2.32. Energy frameworks in HL^{II} ligand based on (a) Coulomb energy, (b) Total energy, (c) Dispersion energy and (d) Total energy (annotated)

Table 2.18. The interaction energies (in kJ/mol) between the HL^{II} ligand molecule and surrounding molecules

	N	Symop	R	Electron Density	E_{ele}	E_{pol}	E_{dis}	E_{rep}	E_{total}	E_{Lat}
🟥	2	x+1/2, -y+1/2, z+1/2	11.60	HF/3-21G	-7.5	-2.3	-17.6	8.4	-18.2	-18.2
🟧	1	-x, -y, -z	8.37	HF/3-21G	-1.9	-2.4	-60.1	23.9	-38.2	-19.1
🟨	2	x+1/2, -y+1/2, z+1/2	11.65	HF/3-21G	-6.1	-0.7	-19.0	12.7	-13.5	-13.5
🟩	2	x, y, z	7.44	HF/3-21G	-1.3	-1.1	-11.6	8.3	-5.8	-5.8
🟩	2	-x+1/2, y+1/2, -z+1/2	7.02	HF/3-21G	-2.2	-1.0	-20.4	6.2	-16.2	-16.2
🟦	2	-x+1/2, y+1/2, -z+1/2	8.10	HF/3-21G	-0.9	-1.4	-18.2	4.2	-14.9	-14.9
🟦	1	-x, -y, -z	7.10	HF/3-21G	-9.2	-4.4	-71.2	27.9	-53.8	-26.9
🟪	1	-x, -y, -z	13.01	HF/3-21G	25.2	-0.4	-13.6	0.0	13.1	6.55
🟪	1	-x, -y, -z	14.89	HF/3-21G	-1.5	-0.6	-7.1	0.0	-8.3	-4.15

Table 2.19. Scale factors for benchmarked energy models of HL^{II} ligand

Energy Model	K_{ele}	K_{pol}	K_{disp}	K_{rep}
CE-HF ... HF/3-21G electron densities	1.019	0.651	0.901	0.811

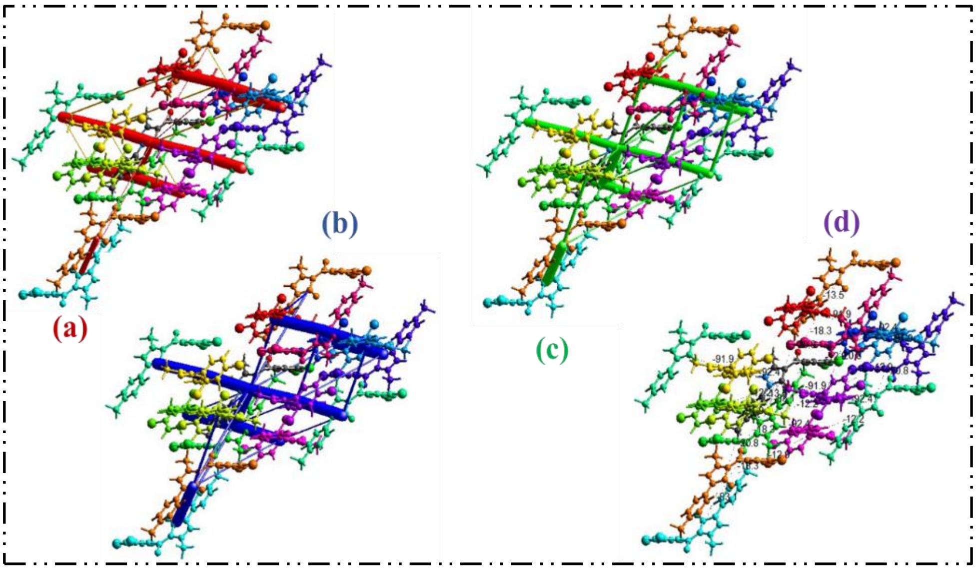

Fig.2.33. Energy frameworks in HL^{III} ligand based on (a) Coulomb energy, (b) Total energy, (c) Dispersion energy and (d) Total energy (annotated)

Table 2.20. The interaction energies (in kJ/mol) between the HL^{III} ligand molecule and surrounding molecules

	N	Symop	R	Electron Density	E_{ele}	E_{pol}	E_{dis}	E_{rep}	E_{total}	E_{Lat}
🟥	1	-	7.36	HF/3-21G	-4.2	-2.8	-25.1	9.8	-20.8	-10.4
🟧	2	x, y, z	12.53	HF/3-21G	-5.8	-4.4	-10.5	0.0	-18.3	-18.3
🟨	1	-	6.27	HF/3-21G	-75.8	-27.7	-67.9	78.9	-92.4	-46.2
🟩	1	-	10.34	HF/3-21G	-3.7	-0.7	-12.8	2.9	-13.5	-6.75
🟩	1	-	12.10	HF/3-21G	-0.2	-1.7	-12.2	0.0	-12.2	-6.1
🟩	1	-x, -y, -z	7.39	HF/3-21G	-38.2	-10.3	-80.7	43.5	-83.1	-41.5
🟩	2	x, y, z	12.12	HF/3-21G	-4.8	-1.1	-5.8	0.0	-10.8	-10.8
🟦	1	-x, -y, -z	17.49	HF/3-21G	-0.9	-0.2	-3.7	0.0	-4.4	-2.2
🟦	1	-	15.26	HF/3-21G	10.7	-0.1	-3.2	0.0	8.0	4.0
🟦	1	-	11.17	HF/3-21G	-4.8	-0.7	-13.4	5.7	-12.9	-6.45
🟪	1	-x, -y, -z	11.73	HF/3-21G	-4.1	-0.7	-10.3	9.5	-6.2	-3.1
🟪	1	-	6.30	HF/3-21G	-71.9	-27.7	-69.8	76.9	-91.9	-45.95

Table 2.21. Scale factors for benchmarked energy models of HL^{III} ligand

Energy Model	K_{ele}	K_{pol}	K_{disp}	K_{rep}
CE-HF ... HF/3-21G electron densities	1.019	0.651	0.901	0.811

2.4 Conclusion

Pyrazoles are important pharmacophores with a wide range of biological activities, and their derivatives exhibit strong pharmacological potential. As a result, their design and synthesis represent a promising area of research. In this study, we have synthesized three novel bidentate acylpyrazolone ligands: HL^{I}, HL^{II} and HL^{III}. All these synthesized ligands have been thoroughly characterized via FTIR and ^{1}H-NMR spectroscopies. The compounds were analyzed using Hirshfeld surface analysis, DFT calculations and single-crystal X-ray diffraction analysis. The exact molecular structure and geometry were confirmed through single-crystal X-ray diffraction and DFT calculations offered details on the electronic structure and reactivity of the compounds. The geometries of all three ligands were optimized using the B3LYP/6-31G basis set, allowing for a thorough analysis of their frontier molecular orbitals in the gas phase. Global index parameters were identified further to understand the systems' physical and chemical features, demonstrating significant correlation and comparison with experimental data. Theoretical bond lengths and bond angles between the ligands match well with the experimental result. In addition to describing intermolecular non-covalent surface interactions with fingerprint plot studies for each of the three ligands, Hirshfeld surface analysis was performed to evaluate crystal strength using interaction energies and energy frameworks. Several interactions were found using Hirshfeld surface analysis.

References

[1] F. Marchetti, C. Pettinari, R. Pettinari, Acylpyrazolone ligands: Synthesis, structures, metal coordination chemistry and applications, Coord. Chem. Rev. 249 (2005) 2909–2945. https://doi.org/10.1016/j.ccr.2005.03.013.

[2] O.G. Idemudia, A.P. Sadimenko, E.C. Hosten, Metal complexes of new bioactive pyrazolone phenylhydrazones; crystal structure of 4-acetyl-3-methyl-1-phenyl-2-pyrazoline-5-one phenylhydrazone ampp-ph, Int. J. Mol. Sci. 17 (2016). https://doi.org/10.3390/ijms17050687.

[3] B.S. Jensen, H. Meier, K. Lundquist, S. Refn, The Synthesis of 1-Phenyl-3-methyl-4-acyl-pyrazolones-5., Acta Chem. Scand. 13 (1959) 1668–1670. https://doi.org/10.3891/acta.chem.scand.13-1668.

[4] F. Marchetti, R. Pettinari, C. Pettinari, Recent advances in acylpyrazolone metal complexes and their potential applications, Coord. Chem. Rev. 303 (2015) 1–31. https://doi.org/10.1016/j.ccr.2015.05.003.

[5] F. Marchetti, C. Pettinari, C. Di Nicola, A. Tombesi, R. Pettinari, Coordination chemistry of pyrazolone-based ligands and applications of their metal complexes, Coord. Chem. Rev. 401 (2019) 213069. https://doi.org/10.1016/j.ccr.2019.213069.

[6] R.C.D. G.H.Jeffery, J.Baddett, J.Mendham, Vogel's textbook of quantitative chemical analysis, n.d. https://doi.org/10.1085/jgp.25.4.523.

[7] I.U. Shaikh, Synthesis , Characterization and Studies on d^{10} Metal Complexes derived from Acyl Pyrazolones, (2020).

[8] I. Shaikh, R.N. Jadeja, R. Patel, Three mixed ligand mononuclear Zn(II) complexes of 4-acyl pyrazolones: Synthesis, characterization, crystal study and anti-malarial activity, Polyhedron. 183 (2020) 114528. https://doi.org/10.1016/j.poly.2020.114528.

[9] M. Travadi, R.N. Jadeja, R.J. Butcher, M.S. Shekhawat, Neodymium based acylpyrazolone complexes: Synthesis and physicochemical characterizations, Inorganica Chim. Acta. 559 (2024) 121766. https://doi.org/https://doi.org/10.1016/j.ica.2023.121766.

[10] M. Travadi, R.N. Jadeja, R.J. Butcher, Uranyl (VI) Mixed-ligand complex synthesis and characterization using 4-acylhydrazone-5-pyrazolone and 4-acylpyrazolone : Covalency , crystal assay , DFT study and Hirshfeld analysis, J. Mol. Struct. 1281 (2023). https://doi.org/10.1016/j.molstruc.2023.135137.

[11] G. Vala, A.A. Puranik, R.N. Jadeja, D. Choquesillo-Lazarte, Solvent Free, Selective

Oxidation of Styrene Catalyzed by Cobalt Acylpyrazolone Supported onto Neutral Alumina: Synthesis and Spectral Characterization, ChemistrySelect. 9 (2024). https://doi.org/10.1002/slct.202304086.

[12] G.M. Sheldrick, SHELXT - Integrated space-group and crystal-structure determination, Acta Crystallogr. Sect. A Found. Crystallogr. 71 (2015) 3–8. https://doi.org/10.1107/S2053273314026370.

[13] G.M. Sheldrick, Crystal structure refinement with SHELXL, Acta Crystallogr. Sect. C Struct. Chem. 71 (2015) 3–8. https://doi.org/10.1107/S2053229614024218.

[14] C.F. Macrae, P.R. Edgington, P. McCabe, E. Pidcock, G.P. Shields, R. Taylor, M. Towler, J. Van De Streek, Mercury: Visualization and analysis of crystal structures, J. Appl. Crystallogr. 39 (2006) 453–457. https://doi.org/10.1107/S002188980600731X.

[15] A. Rudnitskaya, B. Török, T. Dransfield, A B3LYP/6-31+G(d) study of the reaction pathways and conformational preference in a model Chichibabin reaction, Comput. Theor. Chem. 963 (2011) 191–199. https://doi.org/10.1016/j.comptc.2010.10.023.

[16] J. Hollerton, Why the exchangeable proton in NMR spectroscopy doesn’t show the exact position signal or peak according to the convention?, (2021).

[17] K. Nakum, R.N. Jadeja, study of a mononuclear Cu (II) complex with a 4-acyl pyrazolone ligand, 73 (2018) 713–718.

[18] I. Shaikh, R.N. Jadeja, R. Patel, V. Mevada, V.K. Gupta, 4-Acylhydrazone-5-Pyrazolones and their Zinc(II) Metal Complexes: Synthesis, Characterization, Crystal Feature and Antimalarial Activity, J. Mol. Struct. 1232 (2021). https://doi.org/10.1016/j.molstruc.2021.130051.

[19] Y.P. Singh, R.N. Patel, Y. Singh, Crystal structure, configurational and DFT study of nickel(II) complexes with N2O-donor type Schiff base ligand, Indian J. Chem. - Sect. A Inorganic, Phys. Theor. Anal. Chem. 57A (2018) 44–51.

[20] D. Shoba, S. Periandy, M. Karabacak, S. Ramalingam, Vibrational spectroscopy (FT-IR and FT-Raman) investigation, and hybrid computational (HF and DFT) analysis on the structure of 2,3-naphthalenediol, Spectrochim. Acta - Part A Mol. Biomol. Spectrosc. 83 (2011) 540–552. https://doi.org/10.1016/j.saa.2011.09.002.

[21] P.J. Hay, W.R. Wadt, Ab initio effective core potentials for molecular calculations. Potentials for the transition metal atoms Sc to Hg, J. Chem. Phys. 82 (1985) 270–283. https://doi.org/10.1063/1.448799.

[22] M. Travadi, R.N. Jadeja, R.J. Butcher, Synthesis, Covalency Sequence, and Crystal

Features of Pentagonal Uranyl Acylpyrazolone Complexes along with DFT Calculation and Hirshfeld Analysis, ACS Omega. 7 (2022) 34359–34369. https://doi.org/10.1021/acsomega.2c03923.

[23] J.M.M. and R.C.M. PRADEEP KUMAR VISHWAKARMA, Pyrone-based Cu (II) complexes , their characterization , DFT based conformational drift from square planar to square pyramidal geometry, 128 (2016) 511–522. https://doi.org/10.1007/s12039-016-1048-6.

[24] O. V Gritsenko, Koopmans’ theorem and its density-functional-theory analog assessed in evaluation of the red shift of vertical ionization potential upon complexation, Chem. Phys. Lett. (2017). https://doi.org/10.1016/j.cplett.2017.11.019.

[25] M.A. Spackman, D. Jayatilaka, Hirshfeld surface analysis, CrystEngComm. 11 (2009) 19–32. https://doi.org/10.1039/b818330a.

[26] A. Abayneh, T. Gebretsadik, S. Tadesse, M. Thomas, Synthesis, Spectroscopic, Structural Characterization, Conductivity and Electrochemical Studies of a Schiff Base Ligand and Its Copper Complexes, Adv. Chem. Eng. Sci. 08 (2018) 241–254. https://doi.org/10.4236/aces.2018.84017.

[27] J.H. Pandya, M. Travadi, R.N. Jadeja, R.N. Patel, V.K. Gupta, Synthesis, crystal feature and spectral characterization of paeonol derived Schiff base ligands and their Cu(II) complexes with antimicrobial activity, J. Indian Chem. Soc. 99 (2022) 1–8. https://doi.org/10.1016/j.jics.2022.100403.

[28] M. Travadi, R.N. Jadeja, R.J. Butcher, Uranyl(VI) Mixed-ligand complex synthesis and characterization using 4-acylhydrazone-5-pyrazolone and 4-acylpyrazolone: Covalency, crystal assay, DFT study and Hirshfeld analysis, J. Mol. Struct. 1281 (2023). https://doi.org/10.1016/j.molstruc.2023.135137.

[29] S. Barad, K. Chaudhari, H. Roy, R.J. Butcher, R.N. Jadeja, Acylpyrazolone based Square pyramidal Cu(II) complexes: Synthesis, Structural characterization, DFT and antiproliferative properties, Inorganica Chim. Acta. 559 (2024) 121794. https://doi.org/https://doi.org/10.1016/j.ica.2023.121794.

[30] Qiong Wu, Q. Zi, Y. Qiao, Copper(II) Coordination Complex Constructed from Halogenated Tetradentate Schiff Base Ligand: Synthesis, Crystal Structure, and Hirshfeld Surface Analysis, Crystallogr. Reports. 64 (2019) 905–909. https://doi.org/10.1134/S1063774519060166.

[31] P.R. Spackman, M.J. Turner, J.J. McKinnon, S.K. Wolff, D.J. Grimwood, D. Jayatilaka, M.A. Spackman, CrystalExplorer: A program for Hirshfeld surface

analysis, visualization and quantitative analysis of molecular crystals, J. Appl. Crystallogr. 54 (2021) 1006–1011. https://doi.org/10.1107/S1600576721002910.

[32] C.F. Mackenzie, P.R. Spackman, D. Jayatilaka, M.A. Spackman, CrystalExplorer model energies and energy frameworks: Extension to metal coordination compounds, organic salts, solvates and open-shell systems, IUCrJ. 4 (2017) 575–587. https://doi.org/10.1107/S205225251700848X.

[33] Y. Megrouss, S. Yahiaoui, M. Azayez, Z.D. Benyahlou, S.A. Kaas, H. Benaissi, M. Drissi, A. Chouaih, Molecular Structure, Lattice Energy, Hirshfeld Surface and NCI-RDG Analysis, DFT Calculations, and In Silico Molecular Docking of an Imidazole Derivative, Phys. Chem. Res. 12 (2024) 975–990. https://doi.org/10.22036/pcr.2024.448149.2495.